University of Ferrara

Physics and Earth Sciences Department

Ph.D. in Physics

Binder-free porous germanium anode for Li-ion batteries

Advisor:

_____

Prof. Donato Vincenzi

Candidate

_____

Silvio Fugattini

Co-Advisor:

_____

Dott. Damiano Giubertoni

Co-Advisor:

_____

Dott. Remo Proietti Zaccaria

2015-2018 – XXXI cycle

Coord. Prof. Vincenzo Guidi – FIS/01

Abstract (english)

To develop high energy density lithium ion batteries, the use of new electrode materials is required. Germanium is among the possible alternatives to the most commonly used anode, graphite (372 mAh/g), thanks to its four-times higher theoretical gravimetric capacity (1600 mAh/g).

Here is presented a two-step method to produce a binder-free porous germanium anode, depositing the semiconductor on metallic substrates by means of Plasma Enhanced Chemical Vapour Deposition (PECVD) and subsequently performing an electrochemical etching with hydrofluoric acid to create a porous structure.

The Ge-based electrode attained a capacity of 1250 mAh/g at a current rate of 1C (1C=1600 mA/g) and retained a stable capacity above 1100 mAh/g for more than 1000 cycles tested at different C-rates up to 5C.

Both deposition and etching techniques are scalable for industrial production, whose fields of application could be aerospace or medical applications, due to the high cost of germanium as a raw material.

Abstract (italian)

Per sviluppare batterie agli ioni di litio ad alta densità energetica, è necessario l'utilizzo di nuovi materiali elettrodici. Il germanio è una delle possibili alternative all'anodo più comunemente impiegato, la grafite (372 mAh/g), grazie alla sua capacità gravimetrica teorica quattro volte maggiore (1600 mAh/g).

In questo lavoro viene presentato un processo in due fasi per realizzare un anodo in germanio poroso privo di legante (binder), realizzando film di semiconduttore su substrati metallici mediante deposizione chimica da fase vapore assisitita da plasma (PECVD) ed effettuando successivamente un attacco elettrochimico con acido fluoridrico per creare una struttura porosa.

L'elettrodo in germanio poroso ha raggiunto una capacità di 1250 mAh/g ad una velocità di carica/scarica pari ad 1C (1C = 1600 mA/g) mantenendo, inoltre, una capacità stabilmente superiore a 1100 mAh/g per più di 1000 cicli a diversi C-rate fino a 5C.

Sia la tecnica di deposizione che quella di attacco chimico sono scalabili per la produzione industriale, i cui possibili campi di applicazione sono il settore aerospaziale o medico, a causa dell'elevato costo del germanio come materia prima.

Contents

Introduction

Due to the increasing demand for energy consumption, research on **lithium-ion batteries** (LIBs) is a currently very relevant topic. Since the first commercial device developed by Sony in 1991 [1], LIBs have been one of the cutting-edge technologies to store energy, employed in many fields like portable devices, electric vehicles (EV), electric grids, space applications etc.

Despite decades of technological progress, there is still room to improve performance achieved so far and the work presented in this thesis aims to be a breakthrough step in the development of lithium-ion batteries.

Consumers need batteries with higher **gravimetric capacity**—the amount of electric charge stored per unit of mass (mAh/g)—and **energy density** (Wh/kg). These parameters depend mostly on the materials used to realize **anode** and **cathode**, which together with **electrolyte** and **separator** constitute the main parts of an **electrochemical cell**. The goal is to find new electrode materials able to intercalate a higher quantity of lithium ions with respect to the current anodes and cathodes. While the state-of-the-art cathode materials in LIBs are represented by $LiCoO_2$, $LiMn_2O_4$, and $LiFePO_4$, the **anode** intercalation material is usually **graphite** because it is cheap and chemically stable [2]. Nevertheless, finding an alternative solution to graphite is one of the most important challenges to improve battery performances. Graphite has a very low theoretical gravimetric capacity (372 mAh/g) compared, for example, to metallic lithium anode (3860 mAh/g) [1]. Among alternative anode materials, **silicon** and **germanium** feature higher gravimetric capacities with respect to graphite, due to the possibility of forming compounds with a higher content of lithium, i.e. $Li_{22}Si_5$ (4200 mAh/g) and $Li_{22}Ge_5$ (1600 mAh/g) respectively [3]. The major drawback hindering their use in commercial batteries lies in their **volume expansion** during charge/discharge processes (up to 400%) [4], as rigid semiconductor is not able to withstand these volume changes inducing the deteriorating of the cell in few cycles.

A possible solution to improve the **cycle ability** of the cell is to **nanostructure** the semiconductor, making the anode more compliant with the intercalation and de-intercalation of lithium ions [5–7]. Differently, some authors have tried

to add silicon or germanium particles in a carbon matrix, to improve the overall gravimetric capacity of the active material [8–10]. In spite of its lower capacity compared to silicon, germanium is still attractive because owns a higher **electronic conductivity** (10000 times) [7, 11, 12] and **lithium-ion diffusivity** (400 times) [13–15] with respect to Si. However, it is well-known that germanium is more expensive and less abundant than silicon [16] making unrealistic the use of a germanium-based electrode for future mass production of lithium-ion batteries. The field of application of such an anode could be, for instance, medicine (pacemakers) or space applications (satellites, rover, etc...) where it is worth using a more expensive technology to have lighter and long-lasting batteries.

This thesis research developed a **binder-free porous germanium anode** for lithium-ion batteries for which a **patent** has been already filed, within a project financed by the **Italian Space Agency** (ASI) named **ANGELS** (italian acronym that stands for *ANodi in GErmanio nanoporoso per batterie al Litio per applicazioni aeroSpaziali*).

1

Li-ion batteries: basics and perspectives

Since the first battery was invented by the Italian scientist **Alessandro Volta** in 1799 [17], a lot of efforts have been made to find new chemistries able to store more energy. A breakthrough step was the first rechargeable battery developed by **Gaston Plantè** in 1859 [18]—the so-called lead-acid battery—that gave the opportunity to find new applications for accumulators thanks to the possibility of being re-used. Some years later, in 1866, **Georges-Lionel Leclanché** disclosed a new type of **primary**—not rechargeable—**battery** that put the basis for today carbon-zinc and alkaline cells. In 1901 the maiden **secondary**—rechargeable—nickel-cadmium **battery** developed by **Waldmar Jungner** joined the works of Plantè and Leclanché as the most diffused technologies to store electric charge for nearly a century, all of them still used in nowadays commercial devices [19]. However, a relevant improvement of energy density storage was only possible a few decades later, thanks to the exploitation of **lithium** as electrode material.

In this chapter the working principles of lithium-ion batteries and the anode-materials state-of-the-art are discussed. The most common cathode compounds are also introduced to let a better understanding while describing full cells containing semiconductor-based anodes. Separators and electrolytes are not treated, as do not constitute the active part of an electrochemical cell to whom this thesis is mainly interested in. Finally a brief overview of the battery specifications for aerospace applications is depicted, as it constitutes a possible field of application for the anode developed in this thesis work.

1.1   Why lithium

Lithium is currently used both in *primary batteries*—single use only—as long as in *secondary*—rechargeable—batteries.

What led lithium batteries to be among the most widely used power sources for any kind of electric and electronic devices, are essentially the **higher energy density** (Wh/Kg) and **gravimetric capacity** (mAh/g) with respect to other storage systems, as lithium is the **lightest among metals** (molar mass of 6.94 g/mol and specific gravity of 0.53 g/cm^3) [1]. The gravimetric capacity is the amount of charge released by a unit of mass oxidized completely and is defined by Faraday's law as:

$$gravimetric\ capacity = \frac{N * F}{A} \tag{1.1}$$

where N is the number of valence, A is the molar mass and $F = 96485\,C/mol$ $= 26801\,mAh/mol$ is the Faraday constant, i.e. the total charge of an Avogadro number (1 mole) of electrons. Lithium (N=1, A=6.94 g/mol) has a higher gravimetric capacity with respect to other metals employed in energy storage systems such as lead (N=2 and A=207.2 g/mol):

$$gravimetric\ capacity\,(Li) = \frac{N * F}{A} = \frac{1 * 26801}{6.94} \approx 3860\,mAh/g \tag{1.2a}$$

$$gravimetric\ capacity\,(Pb) = \frac{N * F}{A} = \frac{2 * 26801}{207.2} \approx 260\,mAh/g. \tag{1.2b}$$

Moreover, lithium owns a **small ionic radius** that is suitable for diffusion inside the electrochemical cell and it is among the most **electropositive elements**, that leads to high voltage cells. What determines the battery difference of potential is the algebraic difference between the redox potential of the two electrode materials. As reported in fig. 1.1, lithium is one of the element with the lowest reduction potential found in nature, which makes it one of the best candidates to act as anode material inside an electrochemical cell. Given a couple of electrode substances, the one with lower redox potential tends to oxidize (anode) and the one with the highest redox potential tends to reduce (cathode). The voltage of the cell can be calculated as:

$$\Delta V = \text{redox potential (cathode)} - \text{redox potential (anode)} \tag{1.3}$$

In table 1.1 and 1.2 are reported cell voltage, specific energy, and energy density of some of the most common primary and secondary batteries respectively. It is clear how the employment of lithium has improved these features with respect to previous chemistries.

Electrode reaction	E^0, V	Electrode reaction	E^0, V
$Li^+ + e \rightleftharpoons Li$	-3.01	$Tl^+ + e \rightleftharpoons Tl$	-0.34
$Rb^+ + e \rightleftharpoons Rb$	-2.98	$Co^{2+} + 2e \rightleftharpoons Co$	-0.27
$Cs^+ + e \rightleftharpoons Cs$	-2.92	$Ni^{2+} + 2e \rightleftharpoons Ni$	-0.23
$K^+ + e \rightleftharpoons K$	-2.92	$Sn^{2+} + 2e \rightleftharpoons Sn$	-0.14
$Ba^{2+} + 2e \rightleftharpoons Ba$	-2.92	$Pb^{2+} + 2e \rightleftharpoons Pb$	-0.13
$Sr^{2+} + 2e \rightleftharpoons Sr$	-2.89	$D^+ + e \rightleftharpoons \frac{1}{2}D_2$	-0.003
$Ca^{2+} + 2e \rightleftharpoons Ca$	-2.84	$H^+ + e \rightleftharpoons \frac{1}{2}H_2$	0.000
$Na^+ + e \rightleftharpoons Na$	-2.71	$Cu^{2+} + 2e \rightleftharpoons Cu$	0.34
$Mg^{2+} + 2e \rightleftharpoons Mg$	-2.38	$\frac{1}{2}O_2 + H_2O + 2e \rightleftharpoons 2OH^-$	0.40
$Ti^+ + 2e \rightleftharpoons Ti$	-1.75	$Cu^+ + e \rightleftharpoons Cu$	0.52
$Be^{2+} + 2e \rightleftharpoons Be$	-1.70	$Hg^{2+} + 2e \rightleftharpoons 2Hg$	0.80
$Al^{3+} + 3e \rightleftharpoons Al$	-1.66	$Ag^+ + e \rightleftharpoons Ag$	0.80
$Mn^{2+} + 2e \rightleftharpoons Mn$	-1.05	$Pd^{2+} + 2e \rightleftharpoons Pd$	0.83
$Zn^{2+} + 2e \rightleftharpoons Zn$	-0.76	$Ir^{3+} + 3e \rightleftharpoons Ir$	1.00
$Ga^{3+} + 3e \rightleftharpoons Ga$	-0.52	$Br_2 + 2e \rightleftharpoons 2Br^-$	1.07
$Fe^{2+} + 2e \rightleftharpoons Fe$	-0.44	$O_2 + 4H^+ + 4e \rightleftharpoons 2H_2O$	1.23
$Cd^{2+} + 2e \rightleftharpoons Cd$	-0.40	$Cl_2 + 2e \rightleftharpoons 2Cl^-$	1.36
$In^{3+} + 3e \rightleftharpoons In$	-0.34	$F_2 + 2e \rightleftharpoons 2F^-$	2.87

Figure 1.1: *Standard reduction potentials of electrode reactions at 25 °C [20].*

Table 1.1: *Characteristics of some of the most common primary batteries [21].*

	Primary Batteries		
	$Zn/alkaline/MnO_2$	Li/MnO_2	Li/SO_2
Nominal cell voltage (V)	1.5	3.0	3.0
Specific energy (Wh/kg)	154	260	260
Energy density (Wh/L)	461	546	415

Table 1.2: *Characteristics of some of the most common secondary batteries [21].*

	Secondary Batteries			
	Ni-Cd	Lead-acid	NiMH	Li-ion
Nominal cell voltage (V)	1.2	2.0	1.2	3.8
Specific energy (Wh/kg)	40	35	100	200
Energy density (Wh/L)	135	70	235	570

1.2 SEI: Solid Electrolyte Interphase

Before deepening the functioning of lithium batteries, it is necessary to discuss the **solid electrolyte interphase** (SEI). SEI is a passivation layer formed on electrode surfaces from decomposition products of electrolytes. It allows Li^+ transport and blocks electrons in order to prevent further electrolyte decomposition and ensure continued electrochemical reactions. The formation and growth mechanism of the nanometer-thick SEI films are yet to be completely understood, despite it plays a key-role in battery electrochemistry. The lack of reliable in situ experimental

techniques and its complex structure are two of the main obstacles to a fully comprehension of SEI-layer formation mechanism [22]. SEI is still regarded as the most important but least understood component in rechargeable Li-ion batteries [23].

The formation of SEI layer occurs when the redox potential of the electrodes used in a battery lies outside the electrochemical stability window of the electrolyte [22]. It forms mostly during the first charge, but the formation continues slowly and gradually after first cycle until the SEI layer is fully developed [24]. Once it is properly formed, further decomposition reactions with salts and solvents are prevented since electrons cannot transfer to or through the layer.

The SEI layer should be strong or flexible enough to accommodate the volume change of the anode through cycling (expansion during charging and contraction while discharging) [24]. Studies performed on graphite anodes revealed that many are the compounds that remain on the electrode surface as components of SEI layer. The main ones are LiF, Li_2O, Li_2CO_3 (Fig. 1.2) and other insoluble products, while other soluble products from solvent decomposition may diffuse back into the electrolyte. Most reduction processes take place between 0.8 V and 0.2 V vs Li/Li^+ on highly ordered graphite [24].
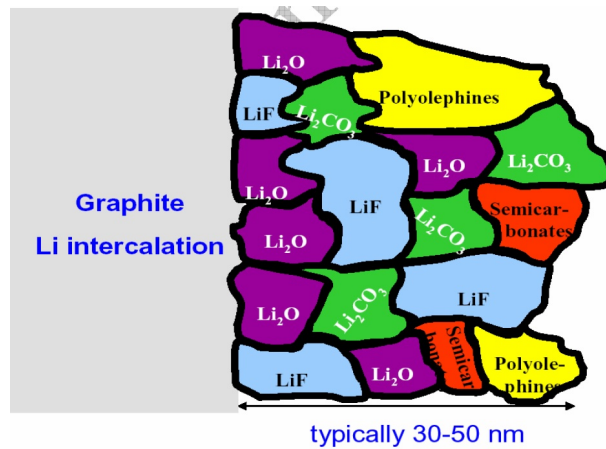
Figure 1.2: *Representative scheme of the solid electrolyte interphase (SEI) [25].*

It is accepted that the SEI layer is essential to the performance of LIBs, and it has an impact on its initial capacity loss, self-discharge characteristics, cycle life, rate capability and safety [24]. To form a stable SEI, is typical the use of electrolyte additives. Their role is essentially sacrificial, as they are reduced at different voltage potentials compared to the base electrolytes to which they are added. The performance enhancement achieved by the use of additives in the base electrolyte of Li-ion batteries is therefore linked to the chemical species formed in their decomposition which are incorporated into the SEI [26].

1.3   Lithium-ion batteries

Lithium was first exploited as metallic anode in primary batteries, with which very high energy density, up to 250 Wh/kg, can be achieved [19]. Subsequently, efforts were done in trying to develop a lithium secondary storage device. Between the end of 1970s and the beginning of the 1980s, some rechargeable lithium batteries were commercialized but this kind of technology showed immediately some safety issues [18]. Faults prevented long battery lifetime, inducing fires and explosions in the worst cases. The main problems occurred during the charge of the battery, because lithium did not plate back homogeneously forming irregularities and dendrites that could induce short circuits (Fig. 1.3). One of the possible solutions
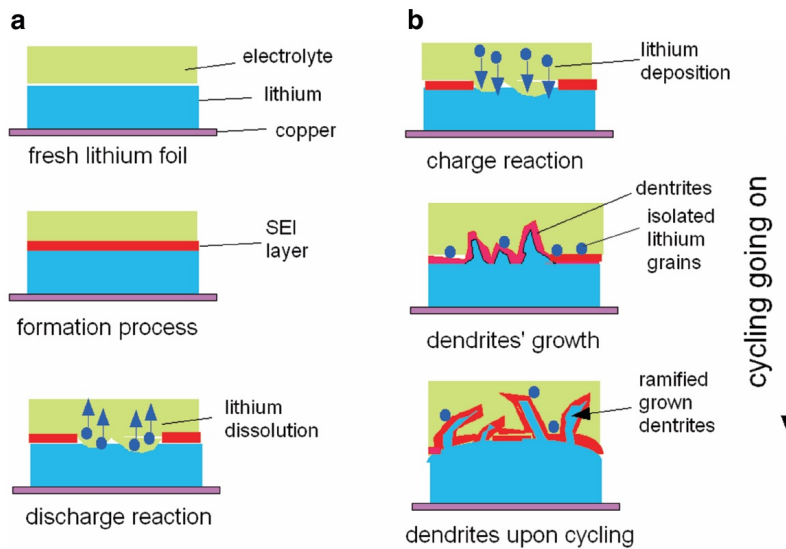
Figure 1.3: *Dendrites formation process in secondary batteries with lithium metal anode [27]: (a) first cycle of discharge and SEI formation (b) dendrites growth upon cycling.*

to overcome this issues was to substitute the lithium metal anode with a more stable and less reactive one. In late 70s **Armand** proposed the idea that turned out to be the basis of the lithium-ion battery: he suggested to create a so-called **rocking chair battery** realized with two different intercalation compounds as positive and negative electrodes, letting lithium ions to transfer from one side to the other [28]. In this way, lithium was still exploited but it was not in a metallic state, improving the safety and the cycle ability of the device. However this costs a significant reduction in energy density, typically around 150 Wh/kg [7], because of the weight of the host intercalation material. First demonstrations of this working principle appeared in the early 80s [29] and the first commercial lithium-ion battery was released by Sony in 1991 [27]. In Fig. 1.4 is depicted the typical working system of a lithium-ion battery that is composed by two intercalation electrodes from which lithium ions shuttle back and forth during charge and discharge cycles.
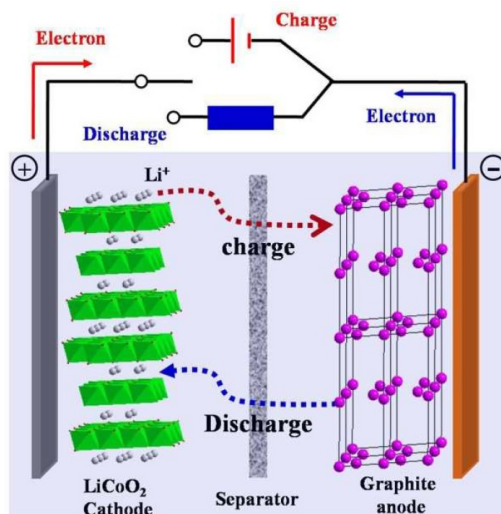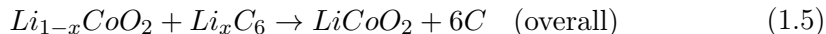
Figure 1.4: *A lithium-ion battery has two intercalation electrodes. Typically the negative one is graphite while the positive one is LiCoO$_2$ [30].*

In Sony's battery, the positive electrode material was **LiCoO$_2$** whereas **graphite** was chosen as negative intercalation compound; both are still among the most used intercalation substances in current commercial devices.

During the discharge of the battery, **graphite** acts as **anode**. Oxidation occurs and lithium ions diffuse from the active material towards the cathode through the separator, while electrons pass into the external circuit powering the load. Meanwhile reduction takes place inside the metal-oxide, accommodating lithium ions that receive electrons by the external circuit. In eq. 1.4 the chemical reactions that take place when the battery releases electric charge are reported, while the reaction in the opposite direction represents the process to store again the energy in the battery.

$$Li_xC_6 \rightarrow xLi^+ + xe^- + 6C \quad \text{(anode)} \tag{1.4a}$$

$$Li_{1-x}CoO_2 + xLi^+ + xe^- \rightarrow LiCoO_2 \quad \text{(cathode)} \tag{1.4b}$$

Coupling eq. 1.4a and eq. 1.4b the overall reaction is obtained:

$$Li_{1-x}CoO_2 + Li_xC_6 \rightarrow LiCoO_2 + 6C \quad \text{(overall)} \tag{1.5}$$

The lithium source lies not only in the cathode, but also into the **electrolyte** that plays a fundamental role to assure the electrical continuity between the two electrodes [16]. Typically, a solution of a lithium salt (lithium exafluorurophosphate LiPF$_6$) is used in a mixed organic solvent (e.g. ethylene carbonate–dimethyl carbonate, EC–DMC) to which several additives can be added to achieve a more stable battery cycling (e.g. VC= vinylene carbonate, FEC= fluoroethylene carbonate).

Finding the best electrolyte solution is also a current research topic [5].

Beside the properties of all the components that constitute a battery, is also important to define parameters that can describe the working conditions of the whole cell like the speed rate at which it is charged or discharged. In fact the power demand of electronic devices is never constant, but often shows peaks of absorption followed by stand-by periods. That is why it is very important to stress electrode materials in different operating conditions, in order to test whether they are reliable for both high and low current needs. The so-called **C-rate** (Cycling rate) is a measure of the cycling speed normalized against the charge stored into the device. A nC rate of charge/discharge means that the cell is charged/discharged in $1/n$ hours, e.g. 1 C means a charge/ discharge cycle in an hour whereas 2 C in 30 minutes [31]. This definition is very useful to find the proper current to be applied in order to test different amounts of the same active materials under the same conditions and allows comparison among different works. Once the C-rate has been established, the corresponding current (I) can be easily obtained

$$I = Q \times nC \tag{1.6}$$

multiplying the charge (Q) stored into the cell by the desired C-rate. If Q is not known, it can be estimated considering the active mass and the theoretical gravimetric capacity of the active material

$$Q = active\ mass\,(g) \times capacity\,(mAh/g). \tag{1.7}$$
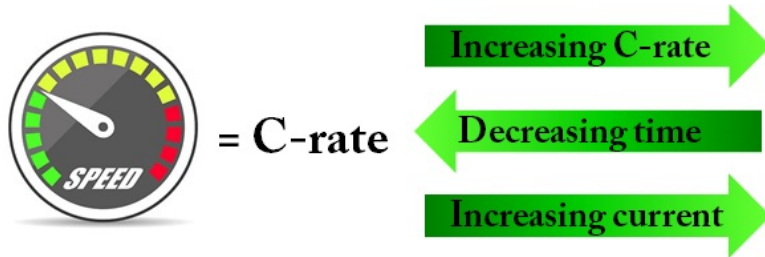
Figure 1.5: *C-rate is a parameter to express the speed at which a cell is charged or discharged, normalized with respect to the amount of charge stored. C-rate is directly proportional to the current and inversely proportional to the time of charging/discharging.*

The C-rate is directly proportional to the current and inversely proportional to the time of charge/discharge (Fig. 1.5). At higher C-rate the active material is more stressed because it is forced to accept or release Li-ions more quickly. In some papers, instead of the C-rate is mentioned the density of current per unit of mass (mA/g), as an alternative way to express the speed of charging/discharging regardless of the active mass [6, 13, 32, 33]. The current density is related to the

time of charge/discharge t—expressed in hours—by this relation:

$$current\ density\,(mA/g) = \frac{capacity\,(mAh/g)}{t(h)}. \qquad (1.8)$$

1.4   Anode materials for LIBs

Graphite is still the reference among LIB anode materials, not only because it was the first intercalation substance used but also because it is even now largely employed as it is cheap and easily processable. A great effort has been done to develop new negative electrode materials but a real alternative to graphite is yet to be found. To be employed as anode, a material must satisfy several requirements such as having low material and production costs, being non-toxic, good ionic and electronic conductor, not soluble in electrolyte and must have a high gravimetric capacity. Furthermore, since the overall voltage of the cell is the difference between the reduction potentials of cathode and anode, the latter must be as close as possible to the Li^0/Li^+ one. Higher cell voltage means higher energy density [34].

Anode substances are generally divided according to the Li storage mechanism into **intercalation materials** like carbon based ones and $Li_4Ti_5O_{12}$, **alloying materials** like Si, Ge, Sn, and **conversion materials** that will not be treated. Particular attention will be given to the discussion of alloying compounds, because is the category to which belongs the negative electrode developed in this thesis work.

1.4.1   Carbon based materials

Graphite is the anode material par excellence, employed as negative electrode since the early 90s and still being the best compromise among all the available anode compounds. It can accommodate one lithium ion every six carbon atoms (LiC_6) with a reversible intercalation process. According to eq. 1.1 the theoretical gravimetric capacity can be calculated as follows:

$$gravimetric\ capacity\,(LiC_6) = \frac{N * F}{A} = \frac{1/6 * 26801}{12} \approx 372\,mAh/g \qquad (1.9)$$

considering N=1/6 and A=12 g/mol. This value is still higher than the capacity for most cathode materials (140-200 mAh/g, see sect. *1.5*). Furthermore one of the most important benefit of graphite is the low reduction potential, only 0.15~0.25 V with respect to metallic lithium. This feature is crucial for obtaining high voltage Li-ion cells [1].

The development of carbon based anodes over the years has mainly consisted in designing properly the device in order to reach the theoretical 372 mAh/g value. The negative electrode is typically a slurry directly spread on a metallic

current collector containing the active material and a binder with the function of agglomerating the compound [20]. However, new alternative materials to graphite are required to overcome its intrinsic limit. Alloying materials are good candidates owing to the great amount of lithium-ions stored, but there are still issues related to the dramatic volume expansions that mine the cycle performances of the cell (see subsect. *1.4.3*).

A compromise is to create a carbon structure having a generic shape and including particles of alloying materials. In this way the good cycle performances and electric conduction of carbon are merged with the high-storage capability of these elements. Furthermore, the significant volume increase can occur inside a compliant matrix without damaging the whole system. Sony in 2005 disclosed a commercial battery with negative electrodes containing nanostructured Sn-Co-C alloy [21, 34]. This is only one example of this approach, quite diffused in both scientific literature and industrial oriented anode materials.

Goriparti et al. [35] presented an inexpensive and simple method to realize carbon-doped TiO_2-bronze nanowires. Here carbon is used as a dopant and not as main component of the active material. This compound showed initially 306 mAh/g at a current rate of 0.1 C keeping a capacity of 106 mAh/g for 1000 charge/discharge cycles at 10 C. Higher performances could be reached coupling semiconductors (Si, Ge) with carbon nanostructure as Botas et al. [9], who developed an active material composed by graphene oxide sheets decorated with silicon nanoparticles ($\sim$50 nm). This compound showed 750 mAh/g of capacity—i.e. twice the theoretical graphite value—for 100 cycles at a quite low current rate (0.026 C) resulting in a charge density of 0.7 mAh/cm^2. Zhong et al. [36] used germanium and graphene creating a 3D nanocomposite that reached 832 mAh/g for 50 cycles at 0.1 C. Even better performances were obtained by Hwang et al. [37] that fabricated a binder-free active material anchoring Ge nanoparticles on multi-walled carbon nanotubes (MWCNT). They showed a capacity of 800 mAh/g at a current speed of 1 C for 200 cycles, i.e. similar to the capacity of Hwang's work but for more cycles and at higher C-rate.

Many patents concerning active materials for negative lithium-ion electrodes are about semiconductor-carbon compounds, like mesoporous carbon composite with Ge/GeO$_2$ particles [38]. Ref. [39] discloses a graphite multi-layer with Ge nano-particles while ref. [40] adds nano-particles of Ge-dioxide to enhance the gravimetric capacity of graphene layers.

All the technical solutions discussed in this subsection are different ways to fabricate active materials with higher gravimetric capacity with respect to graphite, but it is clear how these approaches could never reach the same capacity achievable with pure semiconductor materials (see subsect. *1.4.3*).

1.4.2 $Li_4Ti_5O_{12}$

$Li_4Ti_5O_{12}$ (LTO) is a spinel structure material already used in some commercial batteries [2]. LTO has received much attention because it meets many of the requirements that an anode must have. It is environmentally friendly, relatively cheap and assures very stable cycle performances [41]. This excellent stability is related to the insertion mechanism of lithium ions that causes a negligible volume expansion ($\sim 0.2\%$), leaving the spinel structure almost unaltered [7]. This is why LTO is often considered a "zero strain" material [16]. This noteworthy Li-ion reversible process is also due to the high operational reduction potential—1.55 V vs. Li^0/Li^+—that avoids the formation of dendrites, sometimes observed in carbon based anodes, and mitigates the formation of SEI (Solid Electrolyte Interphase) [34]. The high reduction potential can also be accounted among the drawbacks of LTO together with the low theoretical gravimetric capacity (175 mAh/g) limiting the energy density of the cell. Moreover LTO suffers from low electronic conductivity that could be overcome with proper surface treatments [7].

Although its gravimetric capacity is less than half of the graphite one, the high cycle ability (tens of thousands of cycles) and the high safety of LTO anodes have guaranteed their use in high power applications like grid-energy storage, where long cycle life is required [16, 21].

1.4.3 Alloying compounds

Silicon, **germanium** and **tin**, the elements that follow carbon in the group 14 of the periodic table, are all examples of **alloying materials**. The alloy formed between group 14 elements and lithium assures higher gravimetric capacities with respect to intercalation materials. This is the main reason of the high interest in these materials but also the cause of their main drawback, because the large amount of lithium-ions stored leads to high volume changes hindering the stability of the active compound. There is not a well-defined gravimetric capacity associated to Si, Ge and Sn because the way these materials can lithiate is not unique and several Li-alloys exist. Usually the capacities associated with the ones that have the highest Li/host-material ratio are reported: $Li_{15}M_4$ and $Li_{22}M_5$ where M could be Si, Ge or Sn. According to Faraday's law (eq. 1.1), remembering the molar masses and using respectively N=15/4 and N=22/5 as valence, the theoretical gravimetric capacities of silicon (m_{Si}=28.09 g/mol)

$$Li_{15}Si_4 = \frac{N*F}{A} = \frac{15/4 * 26801}{28.09} \approx 3578 \, mAh/g \qquad (1.10a)$$

$$Li_{22}Si_5 = \frac{N*F}{A} = \frac{22/5 * 26801}{28.09} \approx 4200 \, mAh/g \qquad (1.10b)$$

germanium (m_{Ge}=72.6 g/mol)

$$Li_{15}Ge_4 = \frac{N * F}{A} = \frac{15/4 * 26801}{72.6} \approx 1384 \, mAh/g \qquad (1.11a)$$

$$Li_{22}Ge_5 = \frac{N * F}{A} = \frac{22/5 * 26801}{72.6} \approx 1624 \, mAh/g \qquad (1.11b)$$

and tin (m_{Sn}=118.7 g/mol)

$$Li_{15}Sn_4 = \frac{N * F}{A} = \frac{15/4 * 26801}{118.7} \approx 847 \, mAh/g \qquad (1.12a)$$

$$Li_{22}Sn_5 = \frac{N * F}{A} = \frac{22/5 * 26801}{118.7} \approx 994 \, mAh/g \qquad (1.12b)$$

are easily obtained.

Using Faraday's law to calculate the theoretical capacity for alloys like $Li_{22}Si_5$ neglects the mass of lithium host-ions, dividing the amount of charge stored only by the mass of the hosting-atoms like silicon. Each of them contributes with a valence N=$\#_{Li}/\#_{Si}$ to the overall capacity of the active material. This means that in $Li_{22}Si_5$ alloy, each Si atom can store on average 4.4 electrons while, for instance, only a single electron can be stored by each Li atom in lithium metal anode. This is the reason why the alloy $Li_{22}Si_5$—whose molar mass is higher than lithium one—turns out to have a capacity higher than pure lithium and not lower. It is not inaccurate to neglect the mass of Li-host ions in using Faraday's law, but on the contrary it turns out to be an useful tool to compare different compound performances. Typically what is known is the mass of the unlithiated active material, so values resulting from eq. 1.10, 1.11, and 1.12 are good references to evaluate how far from the theoretical limit is the capacity of the sample currently analyzed.

Silicon is cheap, abundant, environmentally friendly, and has the highest theoretical gravimetric capacity among these three elements. The voltage potential is 0.3-0.4 V above the Li^0/Li^+ redox potential, slightly higher than graphite potential. This implies a smaller cell voltage, but means also higher safety because lithium deposition issues that happen with graphite anodes are avoided. Nevertheless the huge volume expansion up to 420 % induces cracking and pulverization of the active material, hindering its use in commercial devices [34].

Germanium is more expensive, less abundant and has a lower gravimetric capacity with respect to silicon. Nevertheless thanks to its lower band-gap (0.67 eV at 300 K), it owns a higher electronic conductivity (10000 times) [3] and studies performed in mid 50s highlighted a higher lithium-ion solid state diffusivity (400 times) [13–15]. These features, together with a capacity 4 times higher than graphite, raised interest in germanium for new anode materials.

Tin and tin oxide (SnO_2, 783 mAh/g [7]) have already been studied as anode materials because both of them have gravimetric capacities higher than graphite. Nevertheless also tin compounds suffer from huge volume changes (360% when

fully lithiated) and many works have been devoted to overcome this issues [34]. But the future of Sn-based anodes still remain uncertain, because they can hardly compete with the higher performances achievable with silicon and germanium electrodes. This is the reason why the continuation of the discussion will concern only silicon and germanium.

The **phase transformations** that take place during the lithiation and de-lithiation of silicon and germanium are complex phenomenons still object of study. It is not easy to perform in-situ experiments able to observe and describe such a dynamic process, and the results found in literature are not all in agreement with each other. In-situ and ex-situ experiments have shown that the lithiation of crystalline silicon is highly anisotropic while germanium expands mostly isotropically [3] becoming amorphous after the de-lithiation [34]. These properties favour the reversible Li-ions storage mechanism and increased the interest in germanium. Temperature influences the kind of Li-Si alloy, as $Li_{22}Si_5$ is formed at 415°C while $Li_{15}Si_4$ is stable and exists also at room temperature [10]. Concerning the final alloy reached during the lithiation of Ge at room temperature, Yoon et al. described a three step process that led to a coexistence of $Li_{22}Ge_5$ and $Li_{15}Ge_4$ [42]. Baggetto et al. performed XRD measurements that did not show any $Li_{22}Ge_5$ compound but only $Li_{15}Ge_4$ alloy as stated also by Jung et al. that did not observed Li_9Ge_4 either [43,44]. Lim et al. reported $Li_{15}Ge_4$ alloy too while Goward et al. stated the presence of $Li_{17}Ge_4$ distinguishing it from $Li_{22}Ge_5$ [45,46]. A study regarding the phase transformation pathway in function of the current C-rate was performed by Lim et al. [47]. These authors divided the current spectra into three ranges—very low ($\sim$C/21), low ($\sim$C/10), and high ($\sim$1 C)— and proposed a different phase transformation mechanism associated to each of them. Crystalline $Li_{15}Ge_4$ was observed only for low current (C/21) and no $Li_{22}Ge_5$ was detected. Nevertheless a unique model to fully comprehend the lithiation process of germanium is still lacking.

In parallel to phase transition studies, it is interesting to compare the capacities achieved with different semiconductor-based negative electrodes. The challenge to find a cheap, scalable and reliable process to fabricate high capacity electrodes is appealing and a large amount of results can be found among patents and scientific literature. There is a wide range of chemical and physical techniques with which the active compounds can be realized, but the main goal to achieve is the same: to withstand the dramatic volume changes occurring during charge and discharge cycles, a compliant nano-structure is needed.

There are several **parameters** respect to which a comparison can be made. In this work the attention will be focused mainly on the achieved **gravimetric capacity**, the current **C-rate**, and the **number of cycles** for which these performances could be held. When data are available, particular attention will be devoted also to the **areal capacity** (mAh/cm^2) that depends on the amount of active material per unit of area. Increasing the areal capacity allows to miniaturize

cells or to have cells of equal size with enhanced capacity.

A simple three-stage procedure to fabricate porous silicon nano-fibers coated with graphene was developed by Cho et al. [10]. These silicon fibers retained 760 mAh/g capacity after 50 cycles at 0.5 C current rate. Gao et al. attained a higher capacity of 1600 mAh/g for 60 cycles at 0.5 C after having discharged the cell at 0.1 C for the first ten cycles [48]. The anode compound was formed by synthesized silicon nanoparticles (Si NPs) of different sizes, but all of them smaller than 150 nm, which has been considered the threshold to avoid cracking. Three diameters were chosen—130, 90, and 60 nm— and the smallest one showed the best performances thanks also to the use of fluoroethylene carbonate additive (FEC). Ge et al. presented a porous silicon anode showing initially 2900 mAh/g capacity at 0.1 C that never fell below 1100 mAh/g for the next 600 cycles at 0.5 C current rate [6]. To improve the cycle ability of silicon nanotubes (Si NTs), Haro et al. boosted the performances by means of a germanium coating [49]. This treatment allowed to get a 1550 mAh/g capacity with a remarkable areal capacity of 1.2 mAh/cm^2 and Si-Ge NTs retained the capacity over 60% at 3 C rate compared to only 35% delivered by pure Si NTs.

As far as germanium is concerned, the already cited work of Lim et. al reported 1800 mAh/g for 100 cycles but at a very low current rate of C/21 [47]. At higher C-rates the capacity diminished at a value of 1000 mAh/g and 500 mAh/g increasing the current at C/10 and C/5 respectively. Amorphous germanium thin films (60-250 nm) deposited by means of Physical Vapor Deposition (PVD) by Graetz et al., exhibited an astonishing 1700 mAh/g stable capacity for 60 cycles [13]. These results are compatible with the alloy Li$_{22}$Ge$_5$ and the high reversibility of lithiation and de-lithiation was attributed to the nanoscale microstructure of the thin films. Another physical technique was used by Laforge et al. who deposited a 200 nm n-doped germanium film on Cu current collector by means of magnetron sputtering [50]. This thin film exhibited 1465 mAh/g for 180 cycles, very close to the theoretical limit of 1600 mAh/g.

The next reported works are all about active materials that outperformed the previous ones, having lasted for 1000 cycles or more. Kennedy et al. and Chockla et al. dealt with germanium nanowires, while Ngo et al. developed a facile method to prepare 3D nanoarchitectures of Ge coated with a carbon layer (3D-Ge/C) [5, 11, 51]. Kennedy's nanowires were grown by means of VLS (Vapor-Liquid-Solid) technique nucleating from evaporated tin on a stainless steel substrate. Pristine nanowires gradually became a porous network through cycling and retained 900 mAh/g for 1000 cycles at 0.5 C. In Chockla's work Ge nanowires were produced by solution-liquid-solid (SLS) growth using Au nanocrystal seeds. A slurry composed by Ge nanowires, carbon and PVdF (polyvinylidene fluoride) binder was spread on a Cu current collector obtaining an areal capacity of 1 mg/cm^2 corresponding to a thickness of 10 μm. This active compound showed 1248 mAh/g for 100 cycles at 0.1 C, very close to the theoretical capacity of 1384

mAh/g for $Li_{15}Ge_4$ alloy. Furthermore when cycled at a rate of 1 C delivered 600 mAh/g for 1200 cycles and 900 mAh/g when charged at 1 C and discharged at 10 C. 3D-Ge/C structure realized by Ngo et al., exhibited outstanding performances even at higher C-rates. At 0.1 C a high reversible capacity of 1598 mAh/g for 100 cycles was observed and diminished to 1122 mAh/g at 100 C. In addition to that, 3D-Ge/C could withstand 1000 cycles keeping a capacity of 1216 mAh/g at a rate of 2 C, showing 86.8% capacity retention. The areal density of this active material was about 0.5 mg/cm^2.

Nanostructured anode material including semiconductors can be found also among patents. One example is an active material containing nanofibers composed by a germanium core and coated with silicon. This compound is grown by means of VLS (Vapor-Liquid-Solid) technique from a silicon substrate covered with gold nanoparticles deposited by Chemical Vapor Deposition (CVD) [52]. Another active material that contains nano-wires of germanium, silicon or tin is reported in ref. [53]. An active compound composed for 99.99% by silicon structure of whatever shape (nano-tubes, nano-wires, nano-flakes) is described in ref. [54]. A pure germanium negative electrode materials is reported in ref. [55] that regards a porous Ge-layer realized starting from powders. Ref. [56] discloses a 3D structure made of an array of hollow germanium nanotubes using a magnetron sputtering technique.

Alloying material are accounted to be the future of lithium-ion battery anodes and these works testify that this could be the right path to pursue.

1.5   Cathode intercalation materials for LIBs

In the road towards high energy density lithium-ion batteries, research concerning new cathode materials is as important as developing new anodes. The properties that an ideal cathode material should have, are similar to the ones of an ideal anode— high gravimetric capacity, cheap, non-toxic, abundant, etc.— apart from the reduction potential that should be as high as possible to realize high voltage cells. Since the 80s, when the first cathode intercalation compounds for Li-ions have been developed, several materials have been studied and successfully employed in commercial devices. Nevertheless, cathode material is still the limiting factor in the performance of Li-ion batteries, as it offers a lower Li-ion capacity than anodes do [57].

The working principle of an **intercalation crystalline structure** is a solid host network able to store reversibly guest ions. Metal chalcogenides, transition metal oxides, and polyanion compounds are well suited for being used as cathodes in LIBs, although currently research is mainly focused on the last two type of substances due to their higher energy storage capability and operating voltage [16]. In this section a brief review of the main characteristics concerning the

most common cathode intercalation materials will be reported, according to the different crystalline structures they belong to. **Transition metal oxides** exhibit **layered** and **spinel structure** while **polyanion compounds** exist in **olivine** and **tavorite** lattice (Fig. 1.6). An alternative to intercalation compounds are conversion type materials but this thesis will not cover this topic.
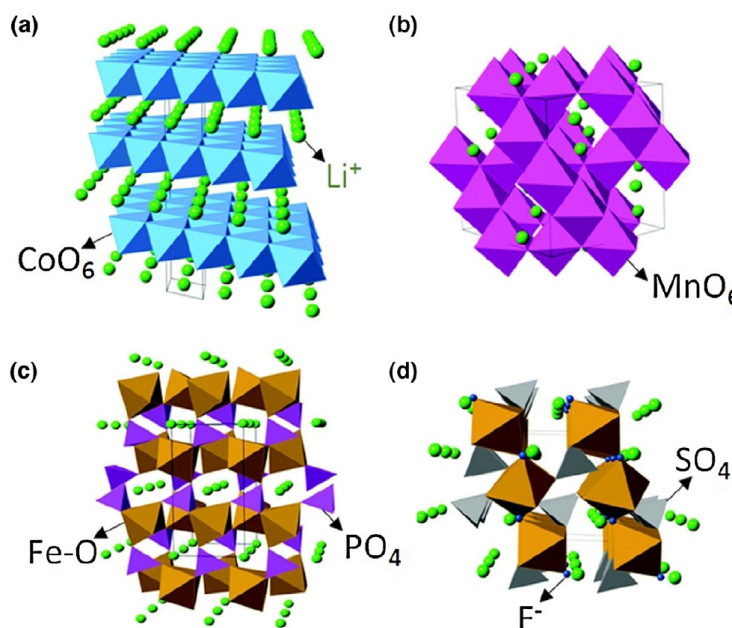
Figure 1.6: *Crystalline structure of (a) layered $LiCoO_2$, (b) spinel $LiMnO_2$, (c) olivine $LiFePO_4$, and (d) tavorite $LiFeSO_4F$ [16].*

1.5.1 Layered materials

Layered materials were the first class of transition metal oxides that have been studied as host network for Li^+ ions since 1980, when J.B. Goodenough introduced **$LiCoO_2$** (LCO) [58,59]. $LiCoO_2$ has a theoretical capacity of 273 mAh/g but in practice only a capacity of 140 mAh/g is obtained as only half of Li ions can be reversibly extracted or inserted into the lattice host [57,60]. In the first commercial lithium-ion battery disclosed by Sony in 1991, LCO was used as cathode material coupled with a graphite anode [18]. Despite being the most used cathode material in commercial Li-ion batteries, LCO has the lowest thermal stability of any other commercial one, is partially toxic, and quite expensive as it contains cobalt [16].

Cobalt can be substituted by nickel or manganese, obtaining respectively **$LiNiO_2$** (LNO) and **$LiMnO_2$** (LMO) layered materials. LNO and LMO own nearly the same gravimetric capacity as cobalt oxide, but the nickel compound, even if it is cheaper, is more thermally unstable and it is still not employed in commercial devices. Manganese is much cheaper and less toxic compared to both Co and Ni but cycling performance of LMO is still not satisfactory, hampering its widespread use [16].

A couple of layered materials widely used in battery market with less content of cobalt are $\mathbf{LiNi_{0.8}Co_{0.15}Al_{0.05}}$ (NCA) and $\mathbf{LiNi_{0.33}Mn_{0.33}Co_{0.33}O_2}$ (NMC). NCA is employed in Panasonic batteries for Tesla electric vehicles (EV) and has a higher capacity ($\sim$200 mAh/g) compared to LCO, but at temperature higher than 40-70°C severe capacity fading may occur. NMC has a gravimetric capacity around 160 mAh/g and a recent work showed a reversible specific capacity up to 243 mAh/g for a macroporous NMC structure [16]. Introduced by Ohzuku's group in 2001, it is an interesting material because of its high reversible capacity and good stability during cycling even at elevated temperature [61, 62].

1.5.2   Spinel materials

Another class of intercalation transition metal oxides are **spinel materials**, whose main example is $LiMn_2O_4$ that has been known since the works of Thackeray et al. in the mid-80s [63, 64]. This spinel Mn-compound has the same benefits as layered $LiMnO_2$, which are lower cost, less toxicity and higher voltage with respect to LCO. However is not easy to synthesize this compound and, to avoid structural distortions when deeply discharged, the theoretical reversible capacity is reduced to 140 mAh/g [65]. Another issue that could cause capacity fading is the partial dissolution of manganese into electrolyte upon cycling that can be circumvented by covering the surface with oxides [60].

1.5.3   Polyanion materials: Olivine and Tavorite

In the search for cheaper and more environmentally friendly cathode materials, **polyanion** compounds like **olivine** and **tavorite** have been studied. Lithium iron phosphate (**$LiFePO_4$**–LFP) is the representative polyanion material having the olivine structure since the work of Padhi et al. in 1997 [66] and it is already in commercial use in batteries for power tools, small vehicles, and Plug-in Hybrid Electric Vehicles (PHEV). LFP has 170 mAh/g capacity, it's cheaper than LCO but the most important property is its higher intrinsic safety, due to the strong P-O covalent bond that excludes any risk of oxygen release. Drawbacks are the low volumetric energy density and the high intrinsic resistance that requires a treatment like carbon coating to ease the electrical conduction [60].

$LiFeSO_4F$ (LFSF) is a tavorite structure material with a quite interesting theoretical specific capacity (151 mAh/g). Currently at a research level, it has gained interest because of its high voltage and the abundance of its components that makes it economical. In addition to that, LFSF has an higher electronic/ionic conductivity. Thus, it does not need any carbon coating [16].

Among all the cathode materials taken into consideration, the choice of the best is not unambiguous but it depends on the specifications of the cells to be made (cell voltage, cycle ability, cost, working conditions, energy density, etc.). In Fig. 1.7 are plotted the discharge profiles of the cathode materials described
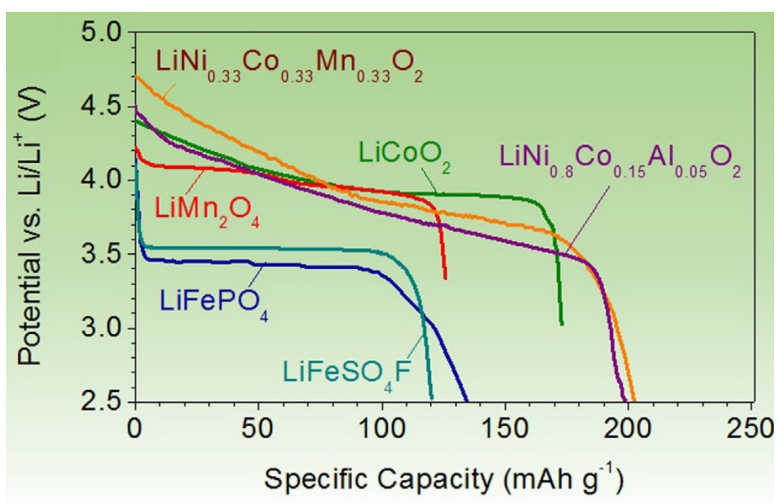
**Figure 1.7:** *Typical discharge profiles of the most common intercalation cathode materials [16].*

Table 1.3: *Characteristics of the most common intercalation cathode compounds [16].*

Crystal structure	Compound	Specific capacity (mAh/g) (theoretical/ experimental)	Level of development
Layered	$LiCoO_2$	274/148	Commercialized
	$LiNiO_2$	275/150	Research
	$LiMnO_2$	285/140	Research
	NCA	279/199	Commercialized
	NMC	280/160	Commercialized
Spinel	$LiMn_2O_4$	148/120	Commercialized
Olivine	$LiFePO_4$	170/165	Commercialized
Tavorite	$LiFeSO_4F$	151/120	Research

in this section and in Table 1.3 their main characteristics are resumed. Fig. 1.8 shows the reduction potentials of some cathode compounds vs lithium metal.

1.6   Full cells with alloying anode materials

All the technical details about anodes and cathodes discussed above, resulted from testing the active materials in prototypes called **half-cells**. This means a complete cell in which the active material to be studied faces metallic lithium as counter-electrode. Lithium foil provides all the Li-ions required from the active compound that can be always fully lithiated during cycling. In this section are
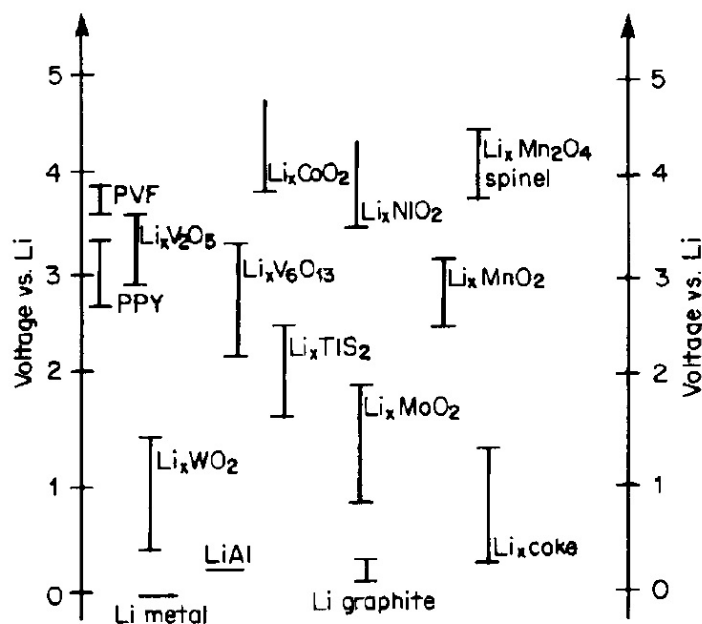
Figure 1.8: *Reduction potential of some cathode materials vs. lithium metal [20].*

examined some papers in which a semiconductor-based anode is coupled with one of the cathode materials cited in sect. *1.5*, assembling what is called **full cell**.

In subsect. *1.4.3* a 3D Ge/C nanoarchitecture developed by Ngo et al. has been already mentioned [51]. The authors not only studied this active material in half-cells but also realized full cells coupling **3D Ge/C** with **LiCoO₂** (LCO) cathode (see subsect. *1.5.1*). The mass ratio between anode/cathode was chosen to have a capacity ratio of anode/cathode of about 0.9 and the cell was tested between 2.2-3.9 V. It showed excellent cycle stability retaining 1479 mAh/g for over 50 cycles at 0.1 C. Another test increasing the C-rate every 5 cycles was performed, resulting in 1200 mAh/g at 1 C and 900 mAh/g at 2 C. Back to 0.1 C the cell delivered again a reversible capacity of about 1491 mAh/g. All the specific capacities reported here refer only to the anode active mass with an areal density of 0.5 mg/cm^2. This full cell was capable of powering a 50-LED bulb array for more than 30 minutes.

Park et al. reported **two full cells**, one realized with **silicon** and one with **germanium nanotube anode**, both of them coupled with **LCO cathode** [33,67]. The first work regards an active material made of **silicon nanotubes** coated with carbon to stabilize the silicon-electrolyte interface. Thanks to the high surface area accessible to the electrolyte, it showed a first discharge capacity of 3247 mAh/g at the 0.2 C rate when tested in half-cell. Pouch-type Li-ion cells having a nominal capacity of 20 mAh were assembled using LCO as cathode. Increasing the current rate from 0.2 C to 5 C the capacity of the anode remained above 3000 mAh/g and the capacity retention after 200 cycles at 1 C was 89%, percentage

comparable to a cell made with commercial graphite. The capacity after 200 cycles was still 10 times higher than commercial graphite batteries when running between 2.75 and 4.3 V. Furthermore, the pouch-cell was disassembled after being cycled and the morphology of silicon nanotubes was found unchanged with respect to pristine active material. The second work is about **germanium nanotubes** synthesized by means of Kirkendall effect [67]. This negative active material showed a reversible capacity of 1002 mAh/g for 50 cycles when tested in coin-type half-cells. Pouch type full cells with nominal capacity of 300 mAh were assembled using LCO cathode. The ratio between negative and positive active mass was 1.01 with a negative areal capacity of 15.15 mAh/cm^2. They were tested between 3 and 4.3 V demonstrating a rate capability of about 40 C for both charge and discharge. In addition to that, several cells accomplished 400 cycles retaining a capacity of 1002 mAh/g with respect to initial capacity of 1020 mAh/g (98% capacity retention). The cell was then disassembled and germanium NTs revealed no observable distortion after battery testing.

Another cathode material that is accounted to give outstanding results with germanium anodes is LiFePO$_4$ (see subsect. *1.5.3*) [34]. Yuan et al. realized a full cell coupling LFP with a negative active material composed by germanium nanowires passivated with alkanethiol [68]. The passivation enhanced Ge nanowires performances that provided 1130 mAh/g when cycled 100 times at 0.1 C in half-cells with an anode mass loading of 1 mg/cm^2. At 11 C current rate the active material still showed 555 mAh/g and a capacity around 1000 mAh/g was recovered when the charge/discharge rate was lowered again at 0.1 C. Furthermore the half-cell was also tested at 55°C and the results obtained were quite similar to room temperature tests, making this material a good candidate for high working temperature batteries. The authors realized a full cell with 1 mg/cm^2 anode mass loading and 8 mg/cm^2 cathode mass loading cycled in voltage window between 2.0 and 3.8 V. After 30 cycles at 0.1 C current rate, the anode gravimetric capacity was around 1000 mAh/g. This cell was able to power separately a green LED, over 60 red LEDs, a white LED, and an audio electronic device. Choi et al. developed a Ge-based anode material that consisted in mesoporous germanium particles prepared by a zincothermic reduction at a mild temperature of 450 °C [69]. The active material was tested in coin-type 2032 half-cells with 10% FEC additive showing interesting results in a wide range of temperatures. At 60°C after 300 cycles at 0.5 C rate, the capacity was 1000 mAh/g corresponding to 60% capacity retention. The best performances were obtained at room temperature providing 1450 mAh/g after 100 cycles at 0.5 C, which is 99.9% capacity retention. At low temperature— -20°C— the loss of capacity was more ample, decreasing up to 556 mAh/g after 50 cycles at 0.5 C rate. But it is worth to note that increasing again the temperature up to 25°C, a capacity of 1264 mAh/g was re-established. The authors assembled a coin-type full cell with a loading density of 1 mA/cm^2, using LFP as cathode. The full cells run in the potential window of 2.0-4.3 V and were

also tested at different temperatures, even if the one cycled at 60°C unfortunately showed a fast drop of capacity. At room temperature it was observed a capacity retention of 70% after 50 cycles at 0.5 C, while an outstanding value of 80% at -20°C in the same conditions was measured.

Full cells with semiconductor anode materials are yet to be commercialized, but encouraging results have already been obtained. The further step will be identifying the most promising and affordable process to be scaled up for mass production.

1.7 LIBs for space applications

Electric energy consumption has always been an issue in space flights that solar panel arrays alone can not manage to satisfy. To survive eclipses when flying around planets or darkness in deep space, satellites and spacecrafts have always needed battery storage systems. The pioneer space batteries were **Nickel-Cadmium** (Ni-Cd), widely employed since the 60s up to mid 80s [70]. Ni-Cd batteries have an energy density around 25 Wh/kg and were mainly chosen due to their high cycle life, as the battery lifespan determines the satellite lifetime. The major drawback of Ni-Cd batteries was the so-called "memory-effect", i.e. the device "remembers" the most used discharge profile and does not work well when asked for something different [70]. Since the 80s came into use **Nickel-Hydrogen** (Ni-H_2) batteries, a new technology properly developed for space applications [20]. The evolved chemistry lead to a higher reliability and longer lifetime in orbit compared to Ni-Cd. Despite still being used today, Ni-H_2 batteries are bulky and occupy a considerable amount of space owing to hydrogen vessels. In 2001 a move away from nickel-based batteries and to a new chemistry began with the flight of Proba-1, the first ESA (European Space Agency) mission having **Li-ion batteries** aboard [71]. They offer a high specific energy of 85-130 Wh/kg, a 3-5 fold improvement in specific energy compared to Ni-Cd cells [72]. In addition the modular concept of Li-ion batteries gives benefits of simplicity while also allowing flexibility in accommodation which was exploited in ESA missions such as Mars Express, CryoSat-2 and Philae. Furthermore Li-ions batteries do not suffer from any memory effect and are also "magnetically cleaner" due to the absence of nickel, which can be significant in sensitive instrumentation. LIBs are the present and the future of space power systems.

Concerning the cycle ability and life duration of the battery pack, there are different requests depending on which orbit the satellite will sit. Earth orbits divide into three main categories: **Low Earth Orbit** (LEO), **Medium Earth Orbit** (MEO) and **Geosynchronous Orbit** (GEO). LEO is a geocentric orbit with an altitude much less than the Earth's radius. Satellites in this orbit are between 80 and 2000 kilometers above the Earth's surface. A MEO satellite sits
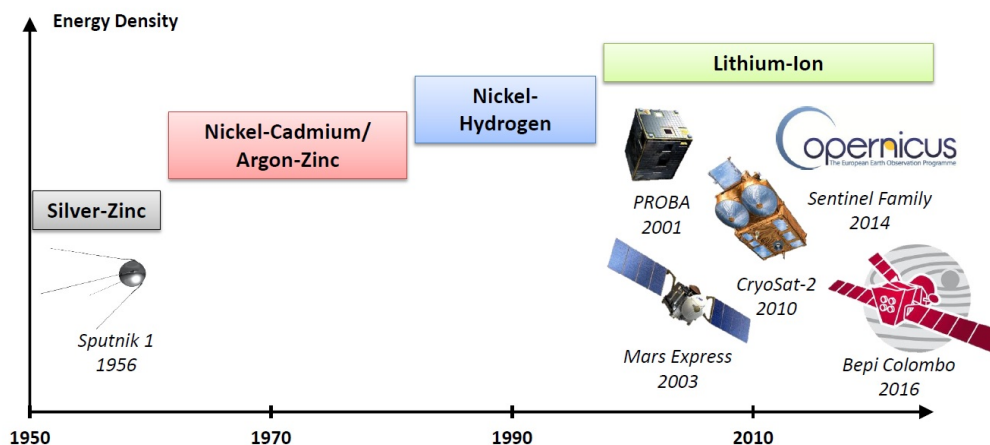
Figure 1.9: *Evolution of the energy density and use in the space field of battery technologies over time [70].*

between 2000 and 36000 kilometers above the Earth's surface, most commonly around 20000 kilometers. GEO is an orbit in which the satellite is always in the same position with respect to the rotating Earth. Satellites in this orbit sit above 35000 kilometers [73]. The main difference between them lies in the number of laps around the earth per day, that is related to the number and the duration of the eclipses and then also the number of cycles the battery has to withstand. A LEO satellites typically makes an average of 6000 cycles/year that turns out to be a cycle requirement of 18000 to 36000 cycles for 3 to 6 years of lifespan. GEO batteries are cycled about 100 times per year and are expected to work for 15 to 20 years, corresponding to 1500/2000 cycles [21]. Hubble space telescope and the International Space Station (ISS) are two examples of LEO satellites, respectively 540 km and 330-440 km above earth [20]. They were both powered by Nickel-Hydrogen batteries until 2017, when ISS was upgraded to lihtium-ion batteries [74]. Li-ion batteries typically have shorter lifetimes than Ni-H$_2$ batteries, as they cannot sustain so many charge/discharge cycles without suffering notable degradation. However, the ISS Li-ion batteries have been designed for 60000 cycles and ten years of lifetime. A proper Battery Management System (BMS) was developed in order to prevent thermal runaway problems that could affect lithium-ion batteries, as happened to Boeing 787 Dreamliner aircraft in 2013 [75].

Space batteries have to work in harsh conditions, in particular as far as temperature is concerned. Low or high temperatures may deeply influence the capacity fading and the cycle ability of the device. The best working conditions for LIBs are between 0°C and 20°C while for Ni-H$_2$ the ideal temperature lies in the range of 15°C [72]. Even if heaters are employed, the NASA thermal cycle requirements is between -20°C and + 40°C [76, 77]. Saft batteries, that owns over 50 years experience in supplying space powering systems, declared that the primary lithium battery installed into the lander Philae of Rosetta mission (2014)

survived for more that 10 years of travel at a temperature less than -60°C [78]. This examples testify how important are temperature tests in space field applications.

Lithium-ion batteries outperformed previous technologies also in space applications. Nevertheless current devices still make use of graphite as anode material [76]. The development of semiconductor-based anode materials could give birth to a new generation of LIBs, making a further leap in battery storage systems.

2

Experimental techniques and methods

In this chapter, experimental techniques and methods for the development of a **binder-free nanoporous germanium anode** for Li-ion batteries are presented.

This Ge-based anode consists in a semiconductor film directly deposited onto a metallic substrate, subsequently nanostructured to realize a compliant matrix able to withstand hundreds of charge/discharge cycles without damaging.

Germanium films have been realized by means of two different deposition techniques, in order to compare the results obtained in either ways. **PECVD** (Plasma Enhanced Chemical Vapor Deposition) and **PVD** (Physical Vapor Deposition) are the two technologies used to deposit thin Ge films, available at University of Ferrara and at Bruno Kessler Foundation of Trento respectively. These equipments were adapted to deposit the semiconductor on metallic substrates and a detailed study to optimise the processes was carried out.

A top-down technique was used to create the germanium porous morphology, preferred to bottom-up methods employed by other authors [11, 52], as quicker and more easily scalable on wider surfaces. SEM characterizations are reported to compare how the porous structure depends on the parameters set while performing electrochemical etching with hydrofluoric acid on bulk Ge-films.

This work aims to develop electrodes with an amount of active mass per unit of area around 0.5-1 mg/cm^2—corresponding to germanium thicknesses up to 5 μm—, which are in line with other Ge-based electrodes found in literature [5, 51]). Furthermore, the use of no binder is convenient, as they are typically used to conglomerate the active material with the disadvantage of increasing the weight of the device without contributing to its energy storage capacity.

2.1 Metallic substrates characterization

Electrodes for lithium-ion batteries are typically composed by an active material deposited onto a metallic substrate acting as current collector. The most common metals used for this purpose are copper, aluminum, and nickel due to their high electric conductivity and low production costs [21]. In this work a different substrate choice was taken because of the working conditions that occur inside PVD and PECVD setups. The most critical environment is in the PECVD reactor, due to the low base pressure (10^{-8} mbar) and the high process temperature (400°C) at which depositions are performed. Substrates with high fusion temperature and low vapor pressure are needed to prevent contamination of the PECVD chamber.

Furthermore, metallic substrates must be resistant to hydrofluoric acid (HF), as germanium samples have to be successively processed with HF electrochemical etching after the deposition.

Molybdenum and stainless steel fulfill these requirements and were employed as substrates for the LIBs anodes developed in this thesis work [79]. These metals are compatible with the environment inside the PECVD reactor as some parts of the reaction chamber itself are made of stainless steel and molybdenum. 99.9% molybdenum and AISI 316 stainless steel foils both 25 μm-thick—provided respectively by Sigma-Aldrich and Goodfellow—have been used. In Fig. 2.1 are reported SEM pictures at different magnifications of these substrates, whose morphology is a consequence of the industrial fabrication methods to realize them. Fig. 2.1a highlights a rougher surface of the molybdenum with respect to stainless steel (Fig. 2.1b). These scratches are still visible after germanium depositions, implying that their depth is comparable with the film thicknesses (1-5 μm). Increasing magnification, details of the molybdenum surface become clearer (Fig. 2.1c-e) while dots with an average diameter of hundreds of nanometers appear on stainless steel (Fig. 2.1d-f).

Despite these substrate morphologies have irregularities of different sizes, neither of the two has induced adhesion issues. Furthermore, a cleaning procedure to remove any organic and greasy trace on the metallic substrates was defined, as residual contaminants of the metallurgical fabrication process were detected. Samples were rinsed in sequence in dichloromethane, acetone, 2-propanol and de-ionized water having a resistivity higher than 18 MΩ/cm.

2.2 PECVD Ge-films

PECVD (Plasma Enhanced Chemical Vapour Deposition) is an equipment available at the Physics and Earth Sciences Department of the University of Ferrara for the deposition of silicon and germanium thin films along with boron as dopant. The plasma enhancement in CVD first emerged in microelectronics because certain
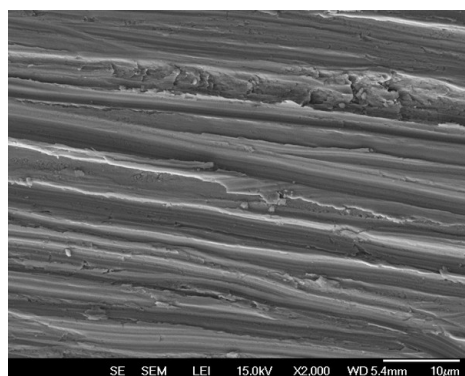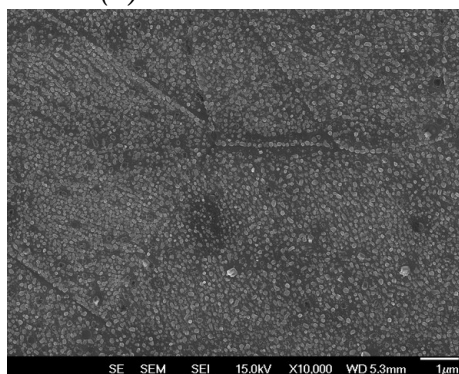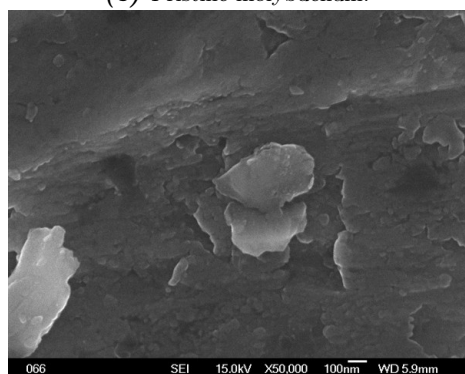
(a) Pristine molybdenum.
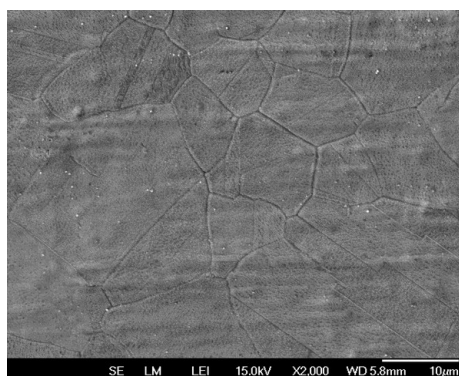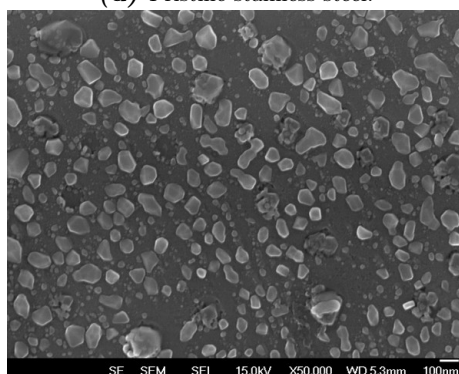

(b) Pristine stainless steel.
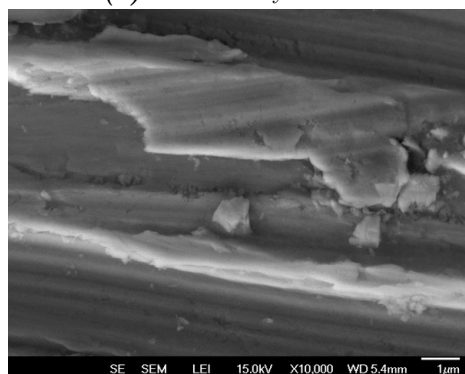
(c) Pristine molybdenum.


(d) Pristine stainless steel.

(e) Pristine molybdenum.

(f) Pristine stainless steel.

Figure 2.1: *Plan view SEM pictures of molybdenum (a,c,e) and stainless steel (b,d,f) at different magnifications. Molybdenum has a rougher surface than stainless steel as can be evinced comparing images of each row that are equally magnified.*

processes cannot tolerate the high wafer temperatures of the thermal CVD. For example, charring of photoresists on patterned wafers is a problem at elevated temperatures of the thermal CVD operation [80]. Furthermore, the energy coming from the plasma glow discharge can lead to higher growth rates with respect to other deposition techniques.
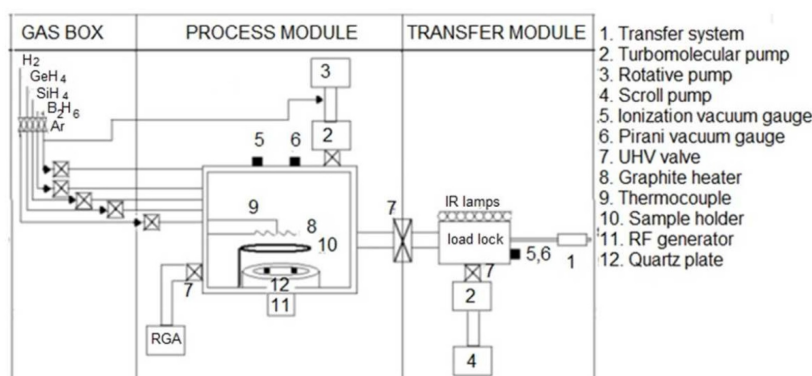
Figure 2.2: *Scheme of the main parts that constitute the PECVD setup with which germanium films were deposited [81].*

In Fig. 2.2 the scheme of the PECVD equipment is depicted. The reactor chamber is a stainless steel chamber kept at a base pressure $P \sim 10^{-8}$ mbar by a vacuum system to prevent any contamination. The system is equipped with a load-lock chamber where the sample is placed before being inserted into the reactor through a gate valve. Infrared lamps promote the desorption of water and other pollutants from the sample while in the load-lock. Just above the sample holder in the main chamber, there is a molybdenum gas ring inlet to provide activation gases (Ar or H_2) and precursor gases as well (GeH_4 or SiH_4). On the top of the chamber the plasma source is placed, consisting in an aluminum antenna that excites the gas molecules at a frequency of 13.56 MHz, a value designated by the international telecommunication authorities not to interfere with other radio transmitted signals. Beneath the sample holder a graphite heater gives the possibility to tune the substrate temperature up to values higher than 450°C.

2.2.1 Preliminary test: PECVD growth rate

PECVD deposition technique allows to obtain a great flexibility of the growth conditions thanks to several parameters than can be set, such as process pressure and temperature, activation and precursor gas fluxes, plasma RF source power etc. At the beginning of this work, it was necessary to study the growth rate in function of some of these variables, as the others were kept constant in order to assure stable deposition conditions. GeH_4 flux (sccm), the power of the radio-frequency (W), and the power of the graphite heater (%) were selected since they have been considered the ones with the strongest effect on the deposition rate. Combining

Table 2.1: *List of growth recipes examined during the PECVD growth rate study.*

Recipe	GeH$_4$ flux (sccm)	Radio-frequency power (W)	Graphite Heater power (%)
1	15	250	15
2	7.5	250	15
3	7.5	250	20
4	15	250	20
5	15	500	20
6	15	250	22
7	7.5	500	20
8	7.5	500	22
9	7.5	250	22

some values for each parameter, a tenth of different growth recipes were established to deposit germanium films (Table 2.1).
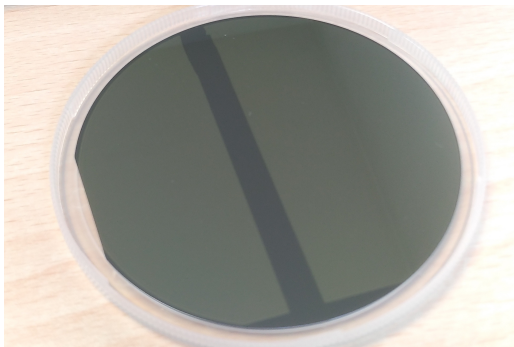

Figure 2.3: *One silicon wafer used to determine the growth rate. The darker strip is the undeposited area while in clearer zones the germanium deposition has taken place.*

To perform accurate growth rate measurements, a stiffer and less rough substrate with respect to metallic foils was required, as molybdenum and stainless steel showed surface structures not negligible if compared to the thickness of germanium films (1-5 μm) (see sect. *2.1*). To overcome this issue, a detailed analysis of the PECVD growth rate using a silicon wafer as a reference was carried out [82]. Silicon has a different emissivity with respect to molybdenum and stainless steel, which may influence the actual temperature reached by the substrate during the process. Nevertheless, as the deposition has started, the emissivity of the sample becomes that of germanium regardless the substrate, so the calculated growth rate is assumed to be substrate-independent. This assumption was confirmed by the fact that Ge-thicknesses of films deposited onto metallic substrates calculated through gravimetric measurements, were—within the confidence interval—in agreement with those expected assuming as growth rate the one calculated through depositions on silicon substrates.

Taking advantage of the stiffness and flatness of Si-wafers, a mask was used during the processes to have a sharp threshold between deposited and undeposited areas on the same wafer (see Fig. 2.3). For every sample, the step height of Ge-film was evaluated with a Wyko NT1100 (Veeco Metrology Group) **interferometer**. Fig. 2.4 is an example of a profilometric measurement based on white light

interferometry in VSI—Vertical Scan Interferometry— mode.
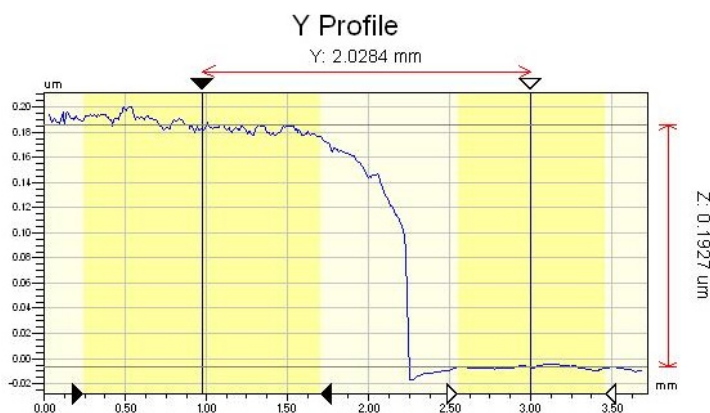
Figure 2.4: *Graph of a profilometric measurements based on white light interferometry in VSI mode. On vertical axes the thickness of Ge-film is extrapolated.*

Film thicknesses measured with interferometer were—within the confidence interval—in agreement with the ones obtained by **SIMS (Secondary Ion Mass Spectrometry)** depth profiles performed at FBK laboratories with a magnetic sector instrument. SIMS is a destructive technique where the sample is sputtered by medium-low energy (15-0.2 keV) primary ions (see Appendix A). A small fraction ($<5\%$) of the sputtered atoms are emitted as (secondary) ions and can be collected by an electric field and discriminated by a mass spectrometer. This can allow the determination of the surface composition in a qualitative way. If the sputtering is carried out in a continuous way and scanning the primary ions on a wide (10-100 um order) square area, a depth profile can be acquired gaining information not only on the surface, but also on the composition in depth. Assuming a constant erosion rate, the sputtering time can be easily converted to depth after measuring the final crater depth by a profilometer. On the other side, the conversion of secondary ion intensity (usually expressed in counts per seconds or arbitrary units - a.u.) to atomic concentration is possible only if an adequate standard is available, i.e. a reference material of matrix composition similar to the sample in exam and with an alternatively determined amount of the species to be quantified [83]. Fig. 2.5 is an example of SIMS depth profile obtained on a Ge-film deposited on silicon substrate. Cesium ions are used as primary beam and secondary ion intensity (a.u.) in function of the depth is reported. The interface between Ge film and Si substrate can be conventionally identified with the depth correspondent to the 50% of the intensity of the Ge-related ion species measured in the film portion of the profile, resulting in a thickness of (146 ± 20) nm. To evaluate the purity of the germanium deposition, the presence of contaminants as oxygen, carbon, hydrogen and fluorine were also monitored although only in a qualitative way due to the lack of adequate standards for these elements in Ge. Hydrogen is the plasma activation

Table 2.2: *Film thicknesses and corresponding growth rates for each of the deposition recipes reported in Table 2.1.*

Recipe	Thickness (nm)	Growth rate (nm/s)
1	182 ± 8	0.91 ± 0.04
2	86 ± 4	0.43 ± 0.02
3	96 ± 4	0.48 ± 0.02
4	185 ± 8	0.925 ± 0.04
5	253 ± 11	1.27 ± 0.06
6	196 ± 9	0.98 ± 0.04
7	138 ± 6	0.69 ± 0.03
8	142 ± 6	0.71 ± 0.03
9	98 ± 4	0.49 ± 0.02

gas and fluorine is contained in NF_3 that is employed as cleaning gas after each PECVD deposition, but neither of them contaminated the semiconductor film.
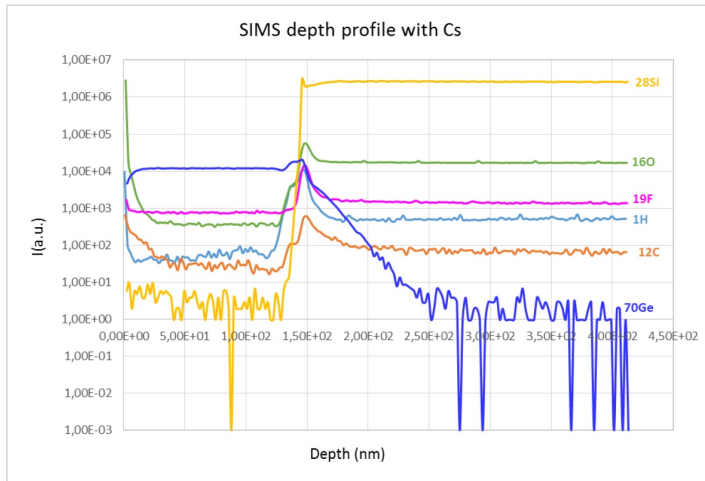
Figure 2.5: *Graph of a SIMS depth profile using cesium ions as primary beam [82].*

Deposition according to each one of the recipes reported in Table 2.1 were performed, keeping constant the process time, (200 ± 1) s. Film thicknesses and corresponding growth rates reported in Table 2.2 are the values obtained by SIMS measurements.

All the anodes discussed in this thesis were deposited using the recipe with the highest growth rate among the ones taken into consideration, which is the recipe n°5 (Table 2.3). The process occurs at a pressure $P \sim 10^{-3}$ mbar and at a temperature higher than 400°C.

Any study regarding the crystallinity degree of the as-deposited germanium films was not carried out, as it is not required for this kind of application. Furthermore, the deposition of germanium films on rough metallic surfaces (Fig. 2.1)

Table 2.3: *Set of parameters chosen for all the anodes deposited in this thesis work.*

| PECVD deposition parameters			
GeH$_4$ flux (sccm)	Radio-frequency power (W)	Graphite Heater power (%)	Growth rate (nm/s)
15	500	20	1.27 ± 0.06

Table 2.4: *Areas of the octagonal mask holes (Fig. 2.6) calculated analyzing the image with ImageJ software.*

A cm^2	B cm^2	C cm^2	D cm^2
6.474	6.490	6.469	6.469

prevents the formation of any monocrystalline layer.

2.2.2 Mask for germanium depositions on metallic substrates

PECVD equipment is designed to deposit semiconductors (silicon or germanium) over 4-inch wafers, while germanium anodes must have a smaller circular size (15 mm diameter) to be tested in 2032 coin-cells (see Chapter 3). It was necessary to design a custom mask to allow depositions of many samples on smaller areas during a single PECVD process. The mask was realized shaping a silicon wafer by means of a high-precision dicing saw (DISCO, DAD3220), as it is a material able to withstand the environmental conditions
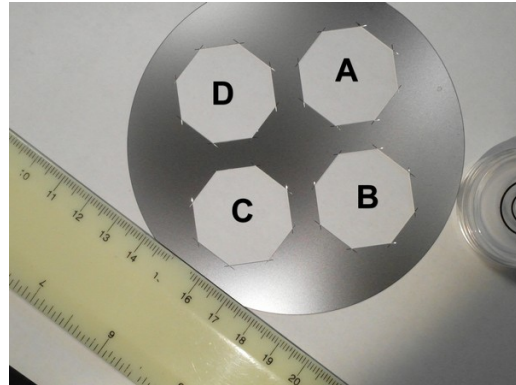

Figure 2.6: *Silicon mask with octagonal holes to deposit four samples simultaneously.*

occurring during PECVD processes without contaminating samples. The holes realized on the mask must be larger than the area on which the etching is performed—a circle of 25 mm diameter, see sect. *2.5*— but not too wide, otherwise metallic substrate would be wasted. As the dicing-machine can carry out only straight cuts, the octagonal shape allowed to use less metallic substrate with respect to polygons with a lower number of sides and to deposit four samples during a single process (Fig. 2.6).

To estimate the germanium mass on the anode area weighting the sample before and after the deposition, it is crucial to know exactly the areas of the four octagons, that were calculated analyzing the image with ImageJ software (Table 2.4). The different regions of the sample can be represented by the scheme reported in Fig. 2.7a. In Fig. 2.7b is shown how a typical sample looks like before the

(a)   (b)
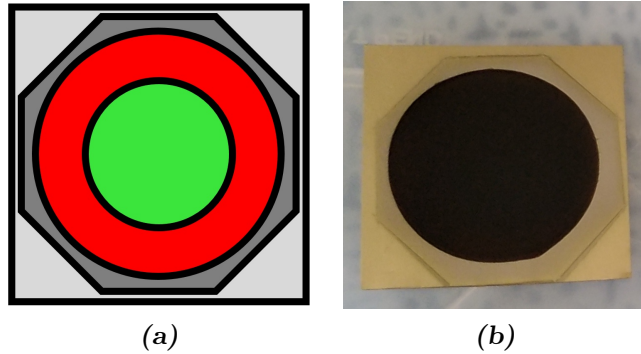
Figure 2.7: *Scheme (a) and picture (b) of one sample. The metallic substrate is a 30 mm × 30 mm square and the octagonal area is the germanium deposition (clearly seen in (b)). The red circle in scheme (a) corresponds to the dark etched area in sample (b) inside which the anode will be hollow-punched (green area in scheme (a)).*

Table 2.5: *Deposition recipe for 1 μm-thick samples.*

PECVD deposition parameters for 1 μm-thick samples				
GeH$_4$ flux (sccm)	Radio-frequency power (W)	Graphite Heater power (%)	Growth rate (nm)	Time (min)
15	500	20	1.27	14

anode is hollow-punched inside the dark etched area.

2.2.3   1 μm and 5 μm samples

The thicknesses of the germanium films were calculated to achieve a required amount of mass on the anode area assuming a growth rate of 1.27 nm/s (see Table 2.3). The goal was to reach a quantity of active mass (i.e. porous germanium) per unit of electrode area in the range of 0.5-1 mg/cm^2, to be comparable with other works [5, 51]. Taking into account that part of Ge will be removed in the etching process, the film thickness was initially established in order to achieve $m = 1$ mg of germanium on the anode area. Assuming an homogeneous deposition on the circular area (d = 1.5 cm) and considering $\rho_{Ge} = 5.325$ g/cm^3 this corresponds to a thickness of

$$h = \frac{m}{\rho S} = \frac{0.001}{5.325\pi(1.5/2)^2} = 1.06\,\mu m. \tag{2.1}$$

Assuming that the growth rate is the same regardless the substrate, the deposition time is easily found to complete the deposition recipe for 1 μm-thick samples (Table 2.5).

To further increase the mass loading assuming that the growth rate does not change during the deposition, a second recipe was established to deposit 5 μm-thick samples, multiplying by a factor 5 the deposition time (see Table 2.6).

It is worth to note that **no binder** and **no adhesion layer** were needed to make germanium stick to the substrate. Binders are substances that typically have

Table 2.6: *Deposition recipe for 5 μm-thick samples.*

PECVD deposition parameters for 5 μm-thick samples				
GeH$_4$ flux (sccm)	Radio-frequency power (W)	Graphite Heater power (%)	Growth rate (nm)	Time (min)
15	500	20	1.27	70

the mere function of conglomerating the active material and making it adhere to the current collector, without playing any electrochemical active role inside the cell [20]. Thus, their use has the disadvantage of increasing the weight of the device without contributing to its energy storage capacity.

### 2.2.4 SEM characterizations

Morphology of the as-deposited Ge-films on metallic current collectors have been studied through SEM (Scanning Electron Microscopy) characterizations. 1 μm-thick films have been deposited on both molybdenum (Ge@Mo) and stainless steel (Ge@SS), to study if the substrate has any influence on the morphology of germanium. As discussed in sec. *2.1*, molybdenum foils have a rougher surfaces compared to stainless steel, still visible after the semiconductor deposition (Fig. 2.8a). Nevertheless the high irregularity of molybdenum foils, probably due to the fabrication process, does not have any influence on the local morphology of germanium. In fact at higher magnifications it can be seen that the film surface is composed by grains with an average size of hundreds on nm regardless the substrate (Fig. 2.8c-d).

To increase the amount of active material per unit of area, thicker samples 5 μm-thick were deposited on molybdenum. The surface of 5 μm-samples presents larger grains with respect to 1 μm films but, despite the greater amount of germanium, there were no adhesion problems.

2.3 PVD Ge-films

PVD (Physical Vapor Deposition) was used as an alternative method to deposit germanium thin films, aiming to compare the results obtained with PECVD-deposited anodes. The equipment present at FBK laboratories (Ulvac EBX-16C with Ferrotec EV S-6 e-gun) is an EBPVD (Electron Beam Physical Vapor Deposition), in which the target material put in a crucible is heated by an electron gun. The resulting vapors spread into the chamber and coat the samples put on a rotating carousel to achieve a more uniform deposition.

Two different batches of Ge-samples 1 μm-thick were deposited with a growth rate of 0.8 nm/s. In the first set germanium was directly grown onto the substrates (Mo and SS), while in the second one metal foils were coated with a 10 nm-thick

(a) *1 μm bulk Ge@Mo.*

(b) *1 μm bulk Ge@SS.*

(c) *1 μm bulk Ge@Mo.*

(d) *1 μm bulk Ge@SS.*
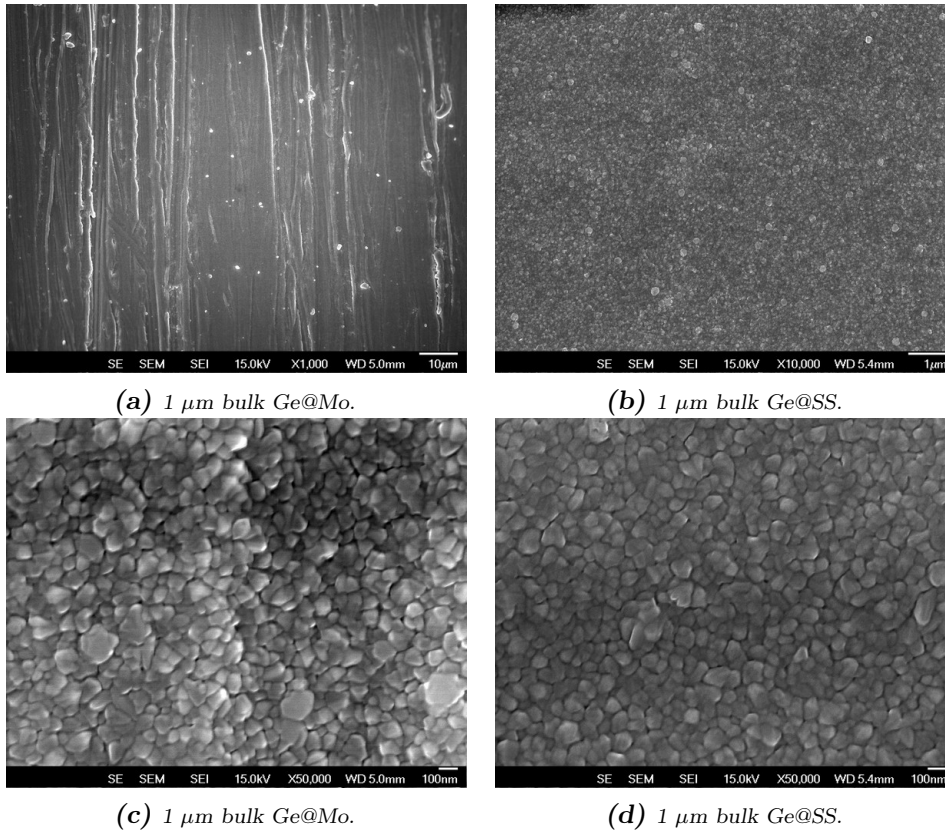
Figure 2.8: *SEM plan views of the as-deposited 1 μm-thick germanium films on molybdenum (a,c) and stainless steel (b,d). The morphology of bare molybdenum substrate (Fig. 2.1a) clearly influences the Ge-film morphology (a), but at higher magnifications (c,d) the grain dimension is similar regardless the substrate.*

(a) *1 μm bulk Ge@Mo.*

(b) *5 μm bulk Ge@Mo.*
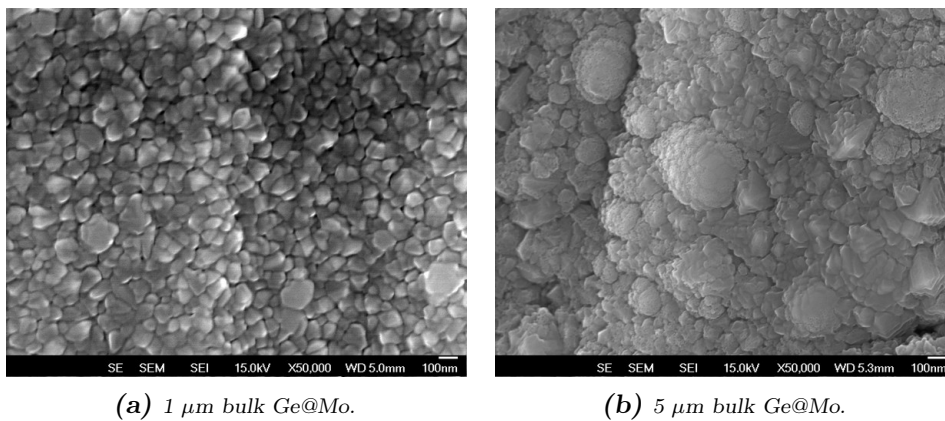
Figure 2.9: *Comparison between 1 μm and 5 μm-thick germanium films on molybdenum. The thicker film looks more grainy with respect to the thinner one.*

adhesion layer of chromium. The Cr-layer was deposited to improve the adhesion of germanium in an attempt to compensate for the low deposition temperature. In this equipment there is not the possibility of setting the substrate temperature, as it is not typically used for this kind of applications. In Fig. 2.10 are reported plan view SEM images to compare morphologies of all the different types of 1 μm-deposition realized in this work. In the first row PECVD films on Mo and SS are taken as reference (Fig. 2.10a-b) while in the second and third row PVD films without and with adhesion layer are reported. All the pictures were taken at the same magnification, from which results a smoother surface of PVD samples on stainless steel (Fig. 2.10d-f) with respect to PECVD ones, apart from some big particles $\sim$400 nm wide. Compositional analysis performed by means of EDX (Energy Dispersive X-ray Analysis) detector embedded in SEM microscope disclosed that these particles are composed of germanium and not of any other contaminants. PVD films on molybdenum without adhesion layer exhibit the roughest surface among all the samples (Fig. 2.10c), while the one with Cr-layer (Fig. 2.10e) showed a surface morphology that resemble SS-grown films. Probably these big Ge-particles are generated by defects acting as nucleation centre, but further investigations are needed to deeply investigate this phenomenon.

To carry out cross-section pictures, samples were mechanically cut. A comparison between SEM cross-section images of the six different samples taken at the same magnification, is reported in Fig. 2.11. A complete detachment of the Ge-layer is observed only in PVD samples without adhesion layer, as shown in Fig. 2.11c-d in which the detached Ge-film can be clearly distinguished from the substrate. In PECVD (Fig. 2.11a-b) and PVD samples with adhesion layer (Fig. 2.11e-f), the semiconductor cracked but mostly remained sticked to the substrate, testifying a better adhesion with respect to PVD samples without Cr-layer.

Even if chromium layer improved the adhesion of germanium, all PVD samples damaged during the etching process (see sect *2.5*), and it was not possible to test PVD germanium anodes in battery prototypes. Improving the adhesion of PVD samples with different adhesion layers or through post-deposition annealing are two of the possible solutions to realize reliable anodes with this deposition technique.

## 2.4   Compositional characterizations

SIMS analysis were carried out to identify the main constituents of germanium film composition and the depth distribution of PECVD and PVD deposited layers. The characterization was carried out in MCs^+ mode, i.e. using Cs^+ as primary ions and collecting positive secondary ions formed by the atoms of interest and the re-sputtered Cs ions. Three samples were analyzed, one deposited with PECVD and two with PVD technique. PECVD Ge-film, whose depth profile is reported in Fig. 2.12, is grown on silicon substrate, as samples used to study the PECVD growth
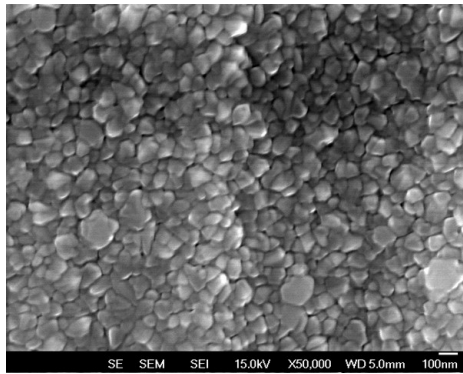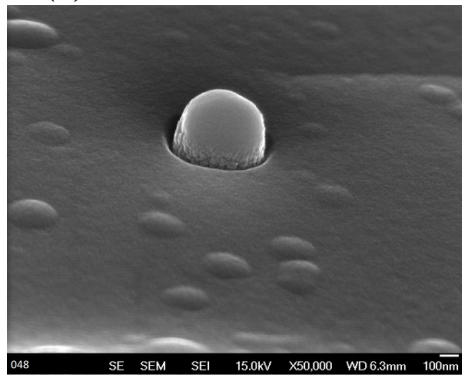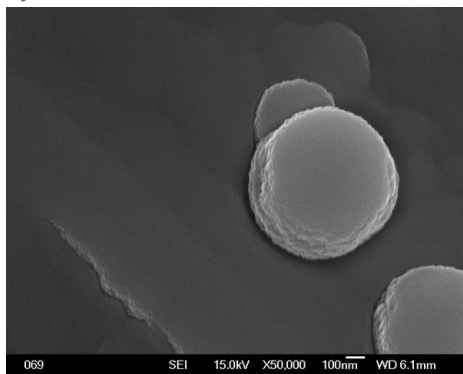
(a) *Mo-substrate: 1 μm PECVD film.*
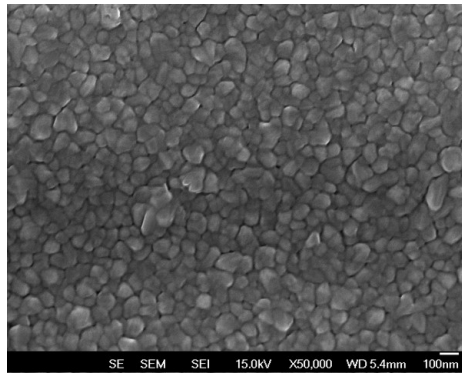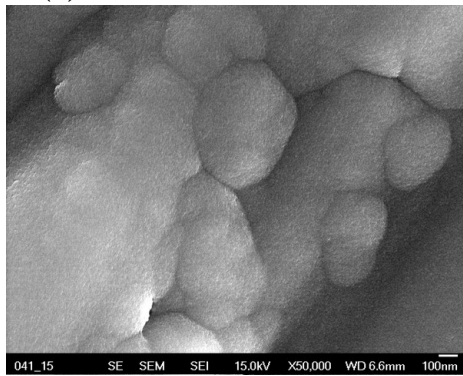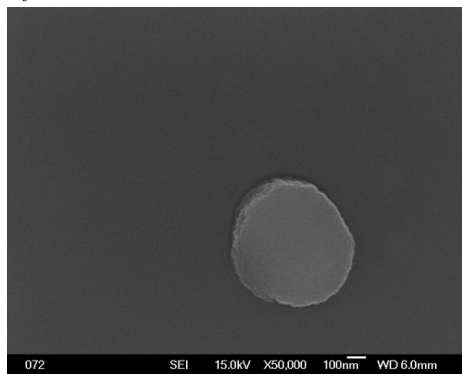

(b) *SS-substrate: 1 μm PECVD film.*

(c) *Mo-substrate: 1 μm PVD film, no adhesion layer.*

(d) *SS-substrate: 1 μm PVD film, no adhesion layer.*

(e) *Mo-substrate: 1 μm PVD film, 10 nm Cr-adhesion layer.*

(f) *SS-substrate: 1 μm PVD film, 10 nm Cr-adhesion layer.*

Figure 2.10: *Comparison between plan views at the same magnification of PECVD, PVD with and without adhesion layer on both substrates.*

(a) *Mo-substrate: 1 μm PECVD film.*

(b) *SS-substrate: 1 μm PECVD film.*

(c) *Mo-substrate: 1 μm PVD film, no adhesion layer.*
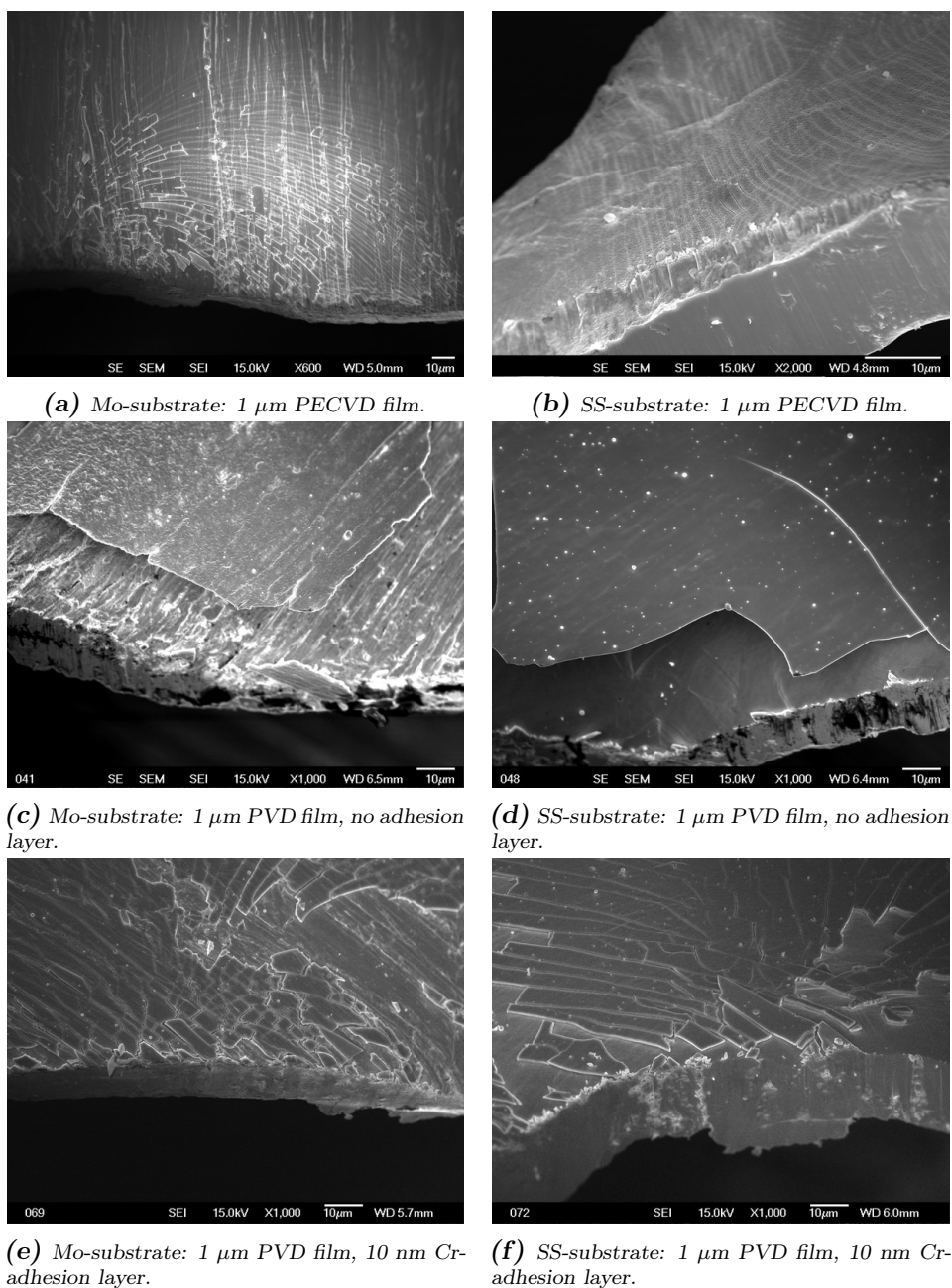

(d) *SS-substrate: 1 μm PVD film, no adhesion layer.*

(e) *Mo-substrate: 1 μm PVD film, 10 nm Cr-adhesion layer.*

**(f)** *SS-substrate: 1 μm PVD film, 10 nm Cr-adhesion layer.*

Figure 2.11: *Cross section SEM images of bulk-Ge samples deposited by means of PECVD (a,b) and PVD technique without (c,d) and with Cr-adhesion layer (e,f) on molybdenum and stainless steel substrates.*

rate (see subsect. *2.2.1*). Nevertheless its composition is considered representative also for PECVD samples deposited on metallic foils, as the reaction occurring inside the PECVD reactor does not depend on the substrate. The two PVD samples were deposited on molybdenum and on stainless steel substrates respectively. As
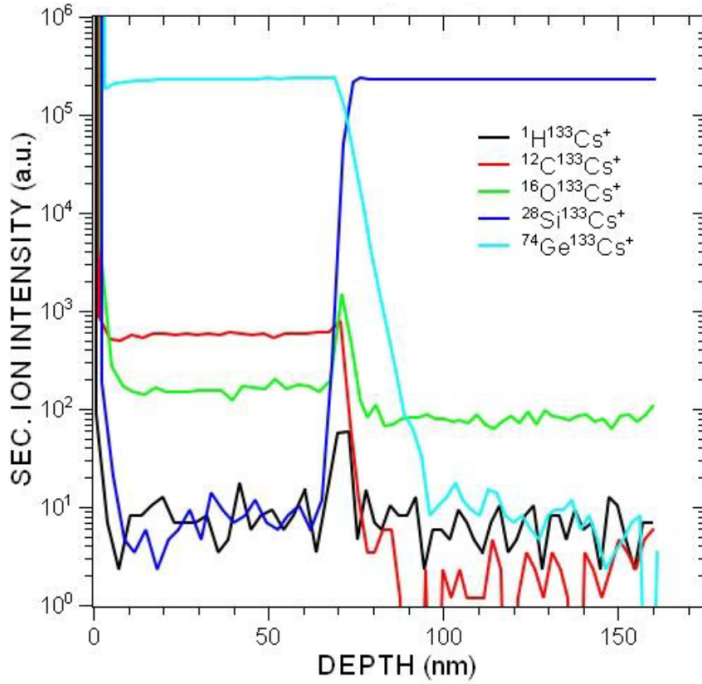
Figure 2.12: *SIMS depth profile of a PECVD-deposited germanium film on silicon substrate.*

expected PECVD-deposited film shows a sharp Ge-Si interface and seems to have a partially oxidized interface between the deposited Ge film and the Si substrate (Fig. 2.12). By contrast, both PVD-samples (Fig. 2.13 and 2.14) have a very wide interface region between Ge and substrate, especially if compared to the film of PECVD sample. This is clearly due to a rough substrate and the consequent lack of a sharp interface between Ge and the metallic foil on which is deposited. In particular, the interface of the one deposited on molybdenum substrate is expected to be rougher than the one grown on stainless steel. This is in agreement with the substrate characterization reported in sect. *2.1*, as the surface of molybdenum foils resulted to be rougher with respect to stainless steel one. Concerning the film composition, the samples deposited by PVD have levels of carbon comparable to PECVD sample, whereas the hydrogen ones are slightly higher. Instead, silicon and oxygen concentrations are much higher, more than an order of magnitude for both species. This is probably due to contaminants present inside the PVD equipment or into the Ge-target used for the deposition.
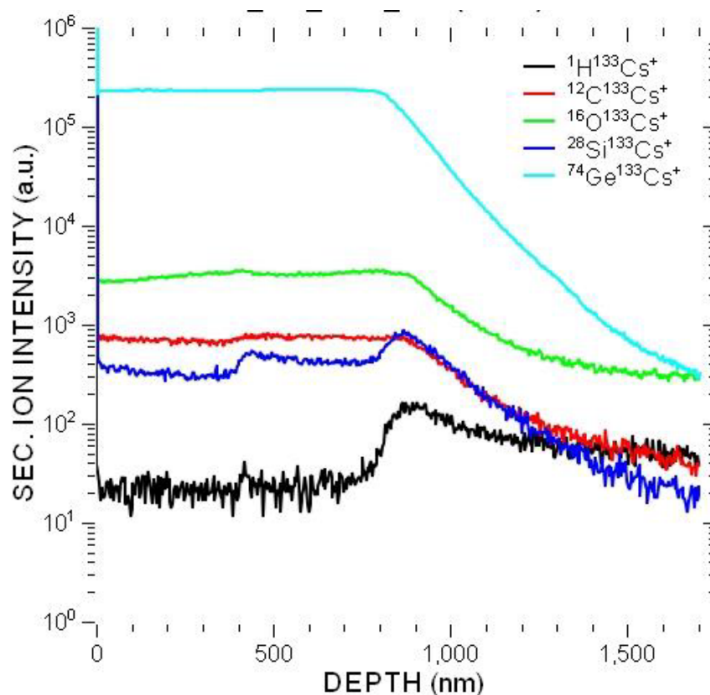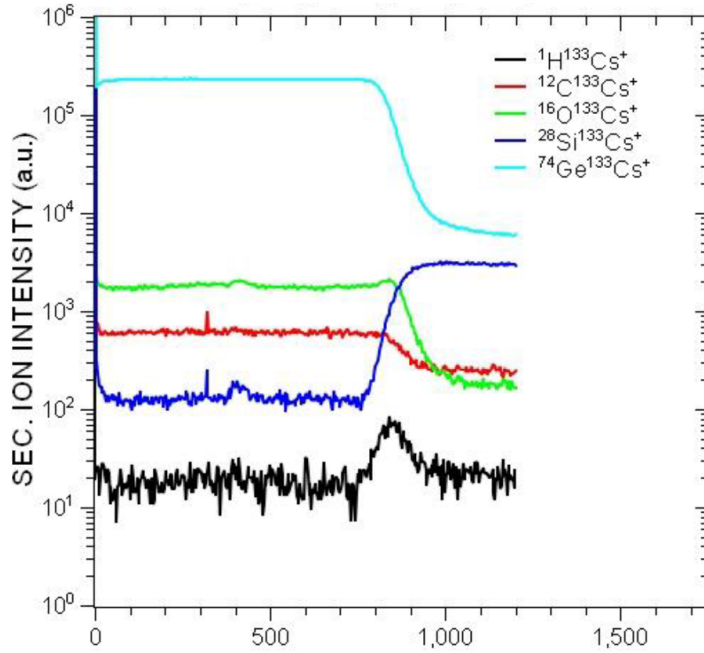
Figure 2.13: *SIMS depth profile of a PVD-deposited germanium film on molybdenum substrate.*

2.5   Nanostructuring samples

Germanium is a very promising anode active material due to its high theoretical gravimetric capacity (1600 mAh/g) but, as discussed in Chapter 1, bulk Ge-films cannot withstand the huge volume expansion induced by the great amount of Li-ions stored. To overcome this issue, the solution adopted in this work is to create a compliant porous structure performing an electrochemical etching with a solution composed by a 3:1 mixture of hydrofluoric acid (HF) diluted at 50% and anhydrous ethanol. Nanostructuring the semiconductor film is the second and last step of the process to realize germanium-based anodes for LIBs presented in this thesis work. The setup used to perform electrochemical etching is showed in Fig. 2.15. It consists in a polytetrafluoroethylene (PTFE) tank sealed with screws and O-rings to an aluminum backplate. The sample is placed in between the two, having the metallic substrate in touch with the backplate and the germanium layer facing towards the inner part of the tank containing the solution. The electrochemical etching is carried out in a galvanostatic mode connecting the negative pole of the generator to a graphite electrode immersed in the solution and the positive pole to the aluminum backplate, as shown in the picture. The etching acts at room temperature on a circular surface of 2.5 cm diameter, corresponding to the red area depicted in the scheme reported in Fig. 2.7a.

Figure 2.14: *SIMS depth profile of a PVD-deposited germanium film on stainless steel substrate.*

2.5.1   1 μm-thick PECVD samples
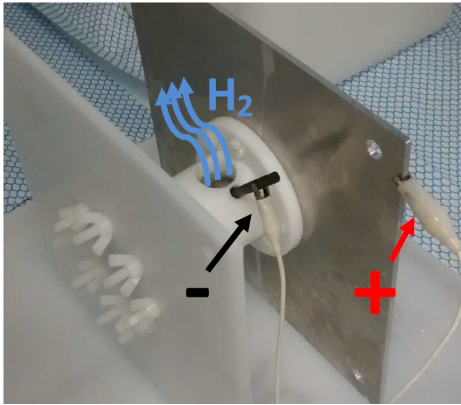
Figure 2.15: *Etching tank to nanostructure germanium anodes [84].*

Anodic dissolution of germanium in highly concentrated HF solutions can be explained through both divalent and tetravalent models, depending on the current density at which the process occurs. For densities below 10 mA/cm^2, the tetravalent dissolution dominates, as four electrons are needed to remove one Ge-atom from the bulk substrate [85]. From previous studies on the porosification of semiconductors conducted at Ferrara laboratories, an etching current of 40 mA was established [81], which corresponds to a density of 8.16 mA/cm^2 and therefore germanium is assumed to dissolve in tetravalent mode. The etching time was calculated to remove half of the Ge-mass from the anode area (0.5 mg), aiming to obtain a 50% degree of porosity. Porosity is defined as the removed mass of germanium divided by the deposited one:

$$Porosity\,(\%) = \frac{mass_{removed}}{mass_{deposited}} * 100. \tag{2.2}$$

Table 2.7: *Etching recipes tested on 1 μm-thick samples using a solution composed by a 3:1 mixture of hydrofluoric acid (HF) diluted at 50% and anhydrous ethanol.*

Etch1			Etch2		
I (mA)	t (s)	Charge	I (mA)	t (s)	Charge
40	180	Q	80	90	Q
Etch3			Etch4		
I (mA)	t (s)	Charge	I (mA)	t (s)	Charge
20	360	Q	40	90	Q/2

Making a proportion between the etching area and that of the electrode, 1.39 mg of Ge have to be dissolved. In a tetravalent regime (N=4), the charge needed to remove such an amount of germanium mass (A=72.64 g/mol) is determined through Faraday's law

$$Q = \frac{mFN}{A} = \frac{0.00139 * 96485 * 4}{72.64} = 7.38\,C \qquad (2.3)$$

and is equal to a time of $t \sim 180$ s with a current $I = 40$ mA.

To deeply investigate the dissolution mechanism—on the basis of the (40 mA, 180 s) recipe—other three etching procedures were tested. Table 2.7 reports the parameters that define the four processes, three of which are different ways to make flow the same amount of charge (doubling or halving current and time) while the latter furnishes only half Q at 40 mA current. This fourth recipe was carried out in order to highlight the dynamic of the germanium dissolution with respect to the elapsed time and to the charge flowed.

Fig. 2.16 reports SEM plan view pictures of porous germanium films on SS substrates realized applying the four etching recipes. By gravimetric measurements, it can be stated that the amount of Ge-mass removed is directly proportional to the charge, regardless the recipe used. In fact, the first three recipes removed the same amount of germanium and the double with respect to the fourth, in which half of the charge was made to flow. The dissolution process that occur is the same and only slightly differences about the surface morphology can be noticed. The porous structure created with etching recipe 1 and 2 are quite similar, showing Ge-pillars with an average dimension of hundreds of nm (Fig. 2.16a and 2.16b). Etching 3 generates wider pillars with respect to the previous two. As it removes the same amount of mass as recipe 1 and 2, probably the slower dissolution process goes deeper instead of creating a finer surface structure (Fig. 2.16c). Pores dug by the 4th etching recipe are less deep and wide because the electrochemical process lasts half of the time (Fig. 2.16d). The dissolution process is dependent on time as expected.

Cross section SEM pictures in Fig. 2.17 give an insight of the dynamic with which the dissolution process create the nanostructure of germanium films. Fig.
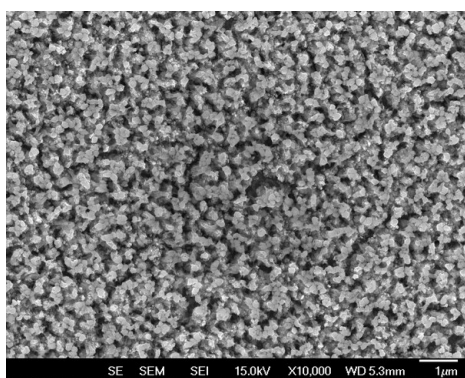
(a) *1 μm-thick porous Ge@SS, etching 1 (40 mA, 180 s).*
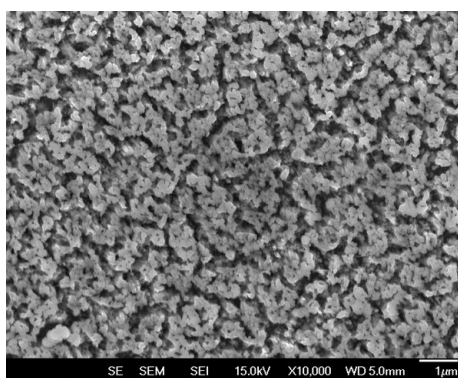
(b) *1 μm-thick porous Ge@SS, etching 2 (80 mA, 90 s).*
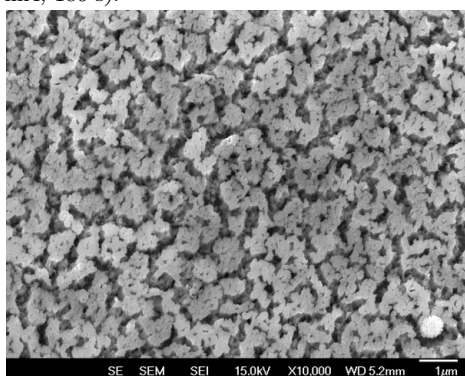
(c) *1 μm-thick porous Ge@SS, etching 3 (20 mA, 360 s).*
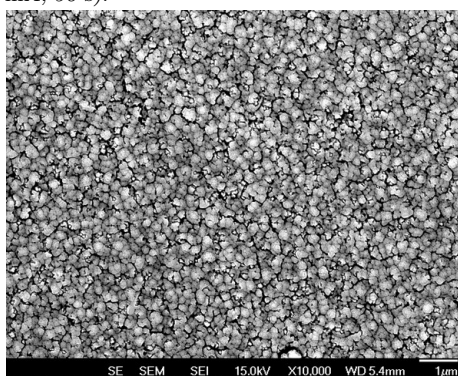
(d) *1 μm-thick porous Ge@SS, etching 4 (40 mA, 90 s).*

Figure 2.16: *SEM plan view pictures of 1 μm-thick porous Ge-films on SS substrate, each of them realized with a different etching recipe.*

(a) *1 µm-thick porous Ge@SS, etching 1 (40 mA, 180 s).*

(b) *1 µm-thick porous Ge@SS, etching 2 (80 mA, 90 s).*

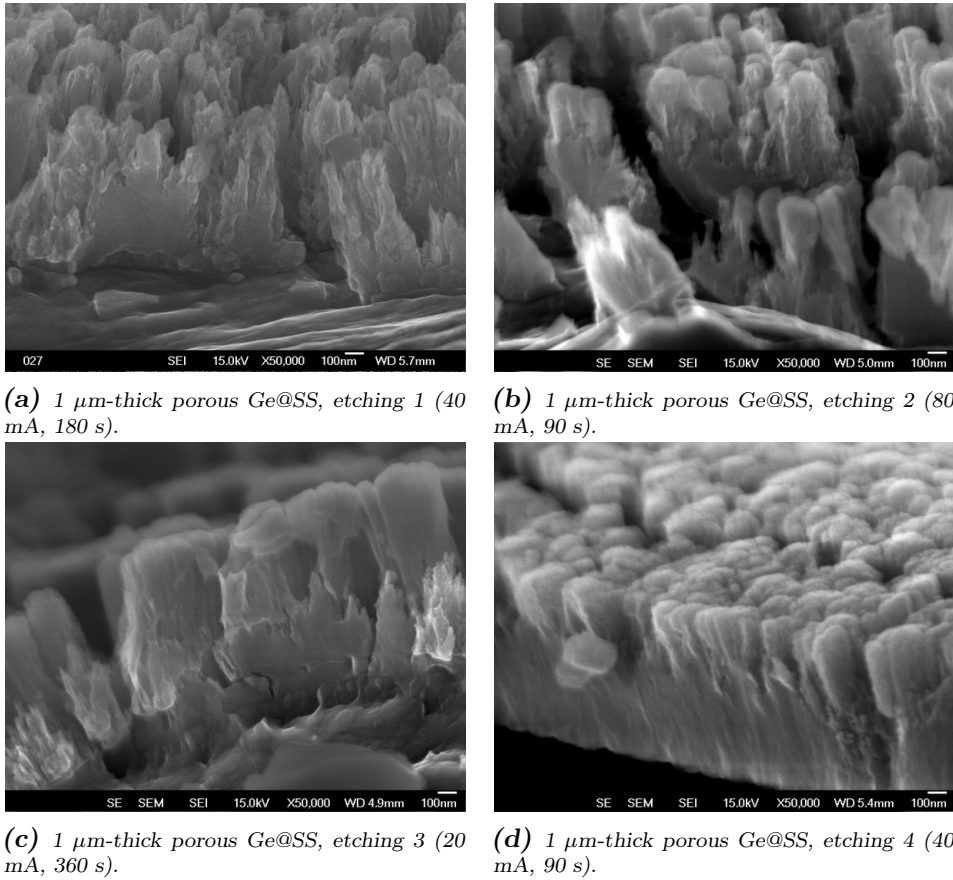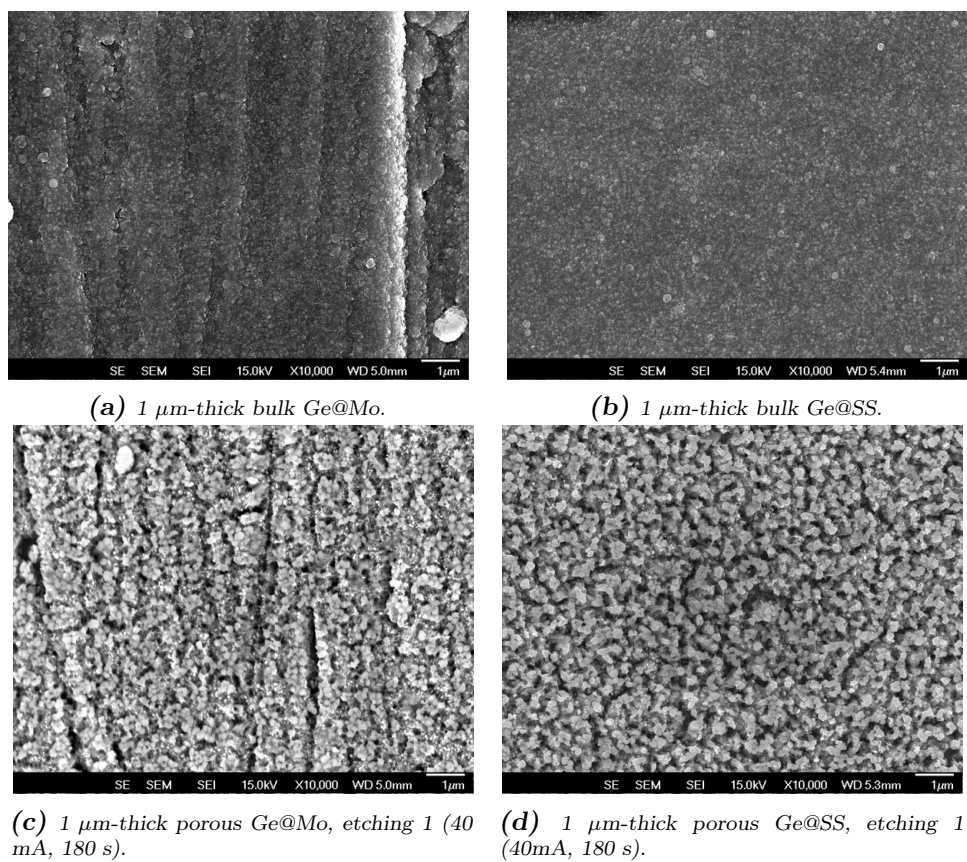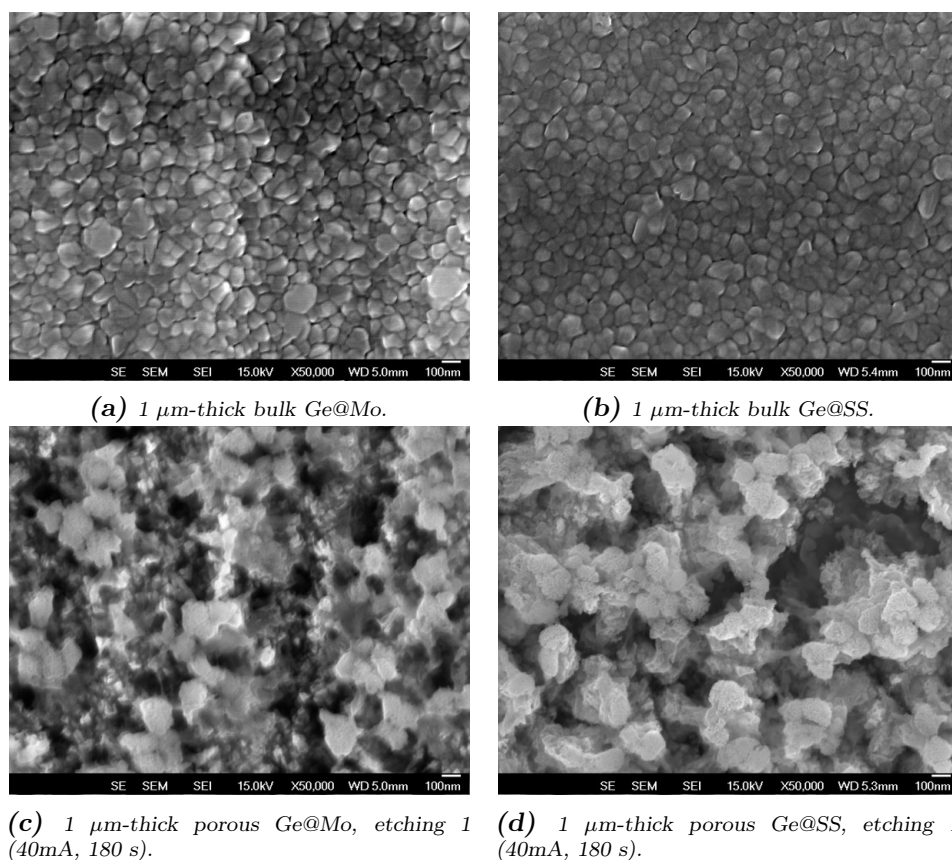**(c)** *1 µm-thick porous Ge@SS, etching 3 (20 mA, 360 s).*

(d) *1 µm-thick porous Ge@SS, etching 4 (40 mA, 90 s).*

Figure 2.17: *SEM cross section pictures of 1 µm-thick porous Ge-films on SS substrate, each of them realized with a different etching recipe.*

2.17d, that is referred to the sample etched with the 4th recipe, clearly shows that only half of the germanium film is still bulk. This means that not only the removed mass is proportional to the charge flown, but also the etching depth is directly related to it. Fig. 2.17a-c confirm that most of the Ge-film is etched when a full-charge etching is released, without compromising the adhesion between the porous film and the metallic substrate. Although the samples were cut mechanically to obtain cross-section images, in no case was observed the detachment of the film, as it had happened with PVD bulk samples (see sect. *2.3*).

The etching recipe 1 (40 mA, 180 s) was performed on germanium films deposited on both metallic foils—molybdenum and stainless steel—to evaluate any substrate-dependence of the porous structure, but gravimetric measurements showed that the amount of Ge-mass dissolved was the same. Fig. 2.18 and 2.19 report comparisons between bulk and porous morphologies at different magnifications of Ge-films deposited on both substrates. Porous films on molybdenum exhibit a less uniform structure than those grown on stainless steel, but this is due to the rougher surface of Mo-foils with respect to SS-substrates—as showed in sec. *2.1*— and not attributed to the etching recipe.

(a) *1 μm-thick bulk Ge@Mo.*

(b) *1 μm-thick bulk Ge@SS.*

(c) *1 μm-thick porous Ge@Mo, etching 1 (40 mA, 180 s).*

(d) *1 μm-thick porous Ge@SS, etching 1 (40mA, 180 s).*

Figure 2.18: *SEM plan view of 1 μm-thick germanium films deposited on molybdenum (a,c) and stainless steel (b,d). The surface morphologies before (a,b) and after (c,d) the electrochemical etching are compared.*

(a) *1 μm-thick bulk Ge@Mo.*

(b) *1 μm-thick bulk Ge@SS.*

(c) *1 μm-thick porous Ge@Mo, etching 1 (40mA, 180 s).*

(d) *1 μm-thick porous Ge@SS, etching 1 (40mA, 180 s).*

Figure 2.19: *SEM plan view of 1 μm-thick germanium films deposited on molybdenum (a,c) and stainless steel (b,d). The surface morphologies before (a,b) and after (c,d) the electrochemical etching are compared at higher magnification with respect to Fig. 2.18.*

The average dimensions of Ge-pillars formed on 1 μm-thick samples are hundreds of nanometers wide in films deposited on both substrates, as shown in Fig. 2.19. This is in line with the average dimension that a porous germanium structure should have to assure a stable cycle ability of the active material [34].

2.5.2   5 μm-thick PECVD samples

Beside the study concerning 1 μm-Ge films, 5 μm-thick samples on molybdenum were deposited, aiming to develop anodes with more active mass per unit of anode area. The etching recipe number one was adapted to thicker films keeping fixed the current (40 mA) and multiplying by a factor five the elapsed time (Tab. 2.8). The removed Ge-mass was five-time the one dissolved with the same recipe performed on 1 μm samples as expected, but the morphology of the structure is quite different.

Each row of Fig. 2.20 reports a comparison of the porous structures obtained on thin (1 μm) and thick (5 μm) films at the same magnification. It is clearly

Table 2.8: *Etching recipe number 1 adapted for 5 μm-thick samples. The solution used is composed by a 3:1 mixture of hydrofluoric acid (HF) diluted at 50% and anhydrous ethanol.*

Etch1 (5 μm)	
I (mA)	t (s)
40	900
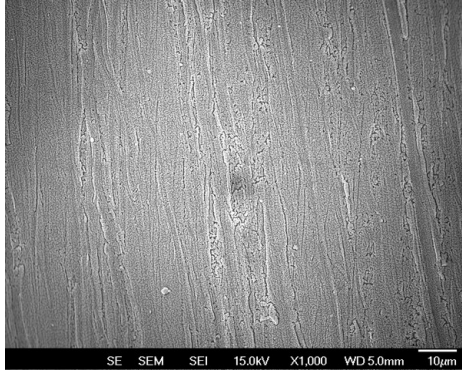
(a) *1 μm-thick porous Ge@Mo, etching 1 (40 mA, 180 s).*
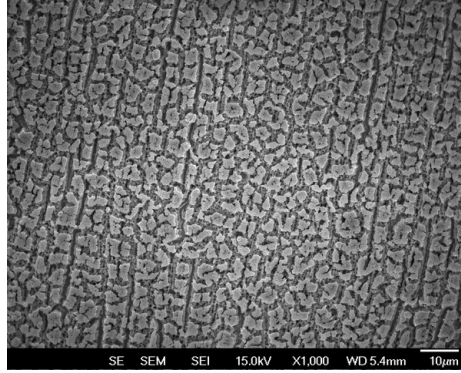
(b) *5 μm-thick porous Ge@Mo, etching 1 (40 mA, 900 s).*
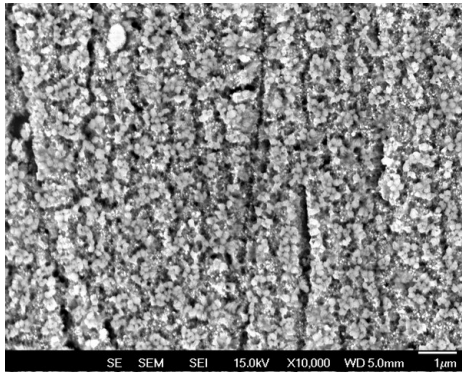
(c) *1 μm-thick porous Ge@Mo, etching 1 (40 mA, 180 s).*
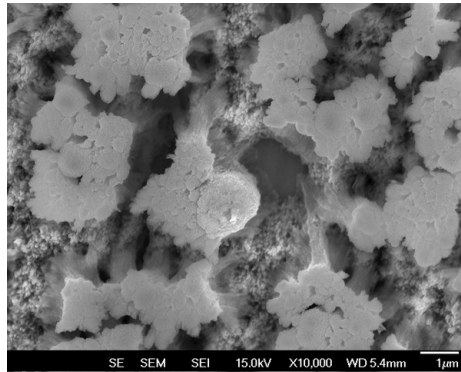
(d) *5 μm-thick porous Ge@Mo, etching 1 (40 mA, 900 s).*

Figure 2.20: *Plan view SEM images of the porous structure obtained with the same etching recipe on 1 and 5 μm-thick Ge-films deposited onto molybdenum substrates.*
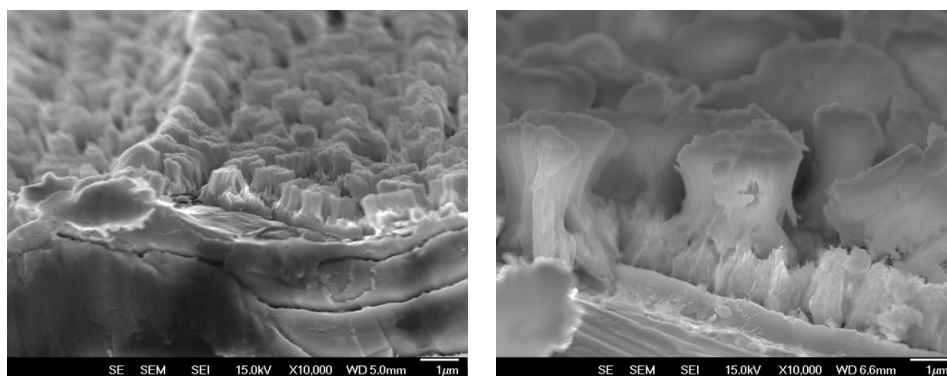
(a) *1 µm-thick porous Ge@Mo, etching 1 (40 mA, 180 s).*

(b) *5 µm-thick porous Ge@Mo, etching 1 (40 mA, 900 s).*

Figure 2.21: *Cross section SEM images at the same magnification of the porous structure obtained on 1 and 5 µm-thick Ge-films deposited onto molybdenum substrates.*

visible that pillars on thick films are nearly ten times larger than the ones on thin films, reaching a width of the order of magnitude of micrometers. Cross section images in Fig. 2.21 show that, also in thicker films, germanium layer is nearly completely etched. Structures of the micron order may be too big to reversibly withstand the volume expansion occurring during the cycle life of the Ge-based anode. As discussed later in Chapter 3, this assumption was confirmed, as battery prototypes with 5 µm-thick anodes did not show the gravimetric capacity and the cycle ability reached by 1 µm-thick anodes. Deeper investigations concerning why Ge-structures on 5 µm-samples are bigger than those observed in 1 µm-thick ones, are needed. Furthermore proper etching recipes for thicker Ge-films are required, in order to perform a finer porous structure in the range of 100 nm also on these samples.

2.6   Conclusions

In this chapter is disclosed a two-step process to realize porous germanium anodes for lithium-ion batteries. The first step is the deposition of a germanium film on a metallic current collector and the second is the nanostructuration of the Ge-layer by means of an electrochemical etching with hydrofluoric acid.

To assure a stable cycle ability when employed in battery prototypes, the average dimension of the Ge-structures must be in the range of hundreds of nanometers [34]. This goal has been achieved with some different etching recipes on 1 µm-thick germanium layers deposited on two different metallic substrates (molybdenum and stainless steel) by means of PECVD (Plasma Enhanced Chemical Vapour Deposition) technique. No binder and no adhesion layers has been needed

between germanium and the metallic current collector, i.e. the mass loading of the anodes is composed only by active material.

PVD (Physical Vapour Deposition) was investigated as an alternative growth method to PECVD, but the adhesion of germanium to the metallic substrates was not enough and samples damaged during the etching processes. Further studies to improve the substrate adhesion of PVD-deposited germanium films are needed. Two possible solution are using different adhesion layers or performing post-deposition annealing process.

Finally, the same etching recipes developed for thin (1 μm) samples were adapted to thicker (5 μm) PECVD-deposited ones. The porous morphology showed pillars ten times bigger than the ones observed in thinner samples, while the target was to obtain structures of the same width. Further studies to realize a finer porous matrix on 5 μm-thick samples are needed, as pillars in the range of hundreds of nanometers [34] are required to develop stable and realiable porous germanium anodes with increased active mass per unit of area.

3

Electrochemical characterizations

Electrochemical performances of porous germanium anodes were characterized at the laboratories of the Italian Institute of Technology (IIT) of Genoa. All the different types of PECVD-deposited electrodes realized with the methods explained in Chapter 2, were assembled in coin-type 2032 half-cells to measure the gravimetric capacity at different C-rates and to assess the cycle ability. Comparisons of the performances in function of the metallic substrate, Ge-thickness and degree of porosity were carried out. In addition to that, the role of two different additives— VC (vinylene carbonate) and FEC (fluoroethylene carbonate)— in improving battery capacity and cycle life was evaluated.

3.1   Half-cells assembly and tests

The term **half-cell** commonly means a cell in which the electrode to be tested is coupled with metallic lithium, which provides Li-ions to fully lithiate the active material while cycling and acts as potential reference of the cell. Assembling half-cells is the standard procedure to test the performances of electrodes and to measure their real gravimetric capacity, i.e. the maximum quantity of lithium that can be stored into the active compound [32].

When dealing with half-cells, attention needs to be paid in what is called *anode* and *cathode*. If the electrode coupled with metallic lithium is devoted—like germanium—to act as anode in full cells, it turns out to be the cathode of the half-cell. The reason is that germanium has a higher reduction potential than lithium, while in full cells it plays the anode role because it is coupled with materials that have higher reduction potential with respect to it (see sect.*1.5*). To avoid confusion, from now on germanium will be generically called *electrode* or *active material*. By
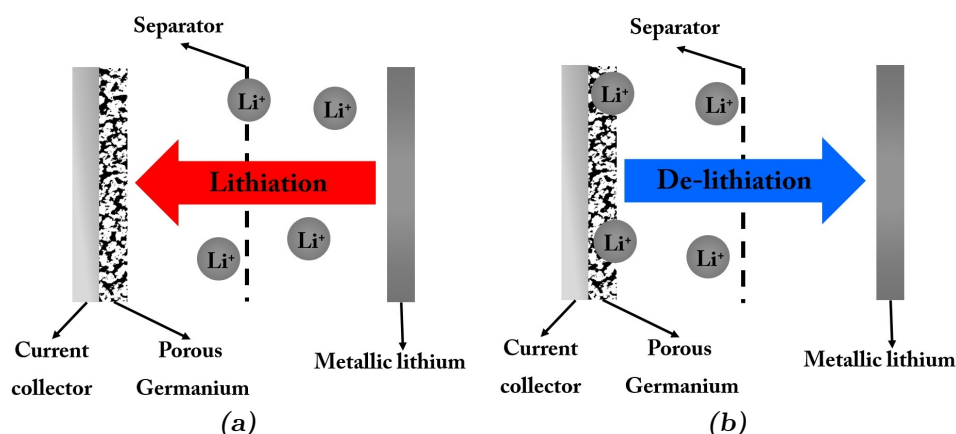
Figure 3.1: *Scheme of lithiation (a) and de-lithiation (b) processes occurring while testing the porous germanium active material in a half-cell.*
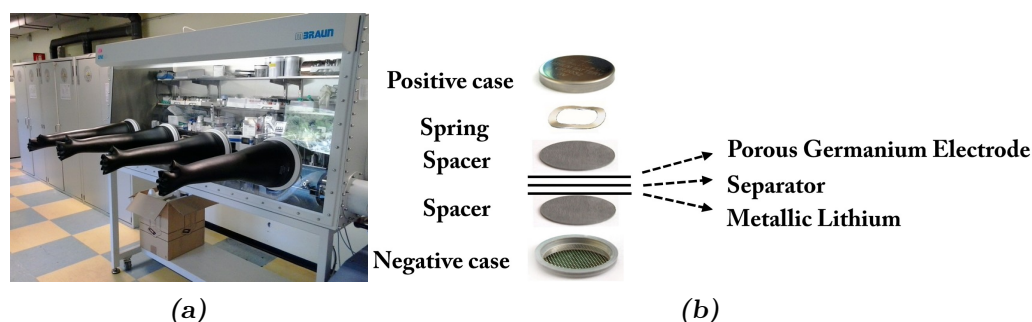
Figure 3.2: *Glovebox (a) inside which coin type half-cells (b) were assembled.*

inverting the role of anode and cathode, the concepts of charge and discharge are also reversed. In fact discharging an half-cells implies reducing germanium, while during the discharge of a full cell it oxidizes. This ambiguity is simply overcome speaking about germanium **de-lithiation** and **lithiation** instead of charge and discharge (Fig. 3.1). Germanium lithiation corresponds to the discharge process in half-cells while it occurs during the charge of a full cell and vice versa for the de-lithiation. Lithiation is the process in which Li-ions enter into the porous active material, while de-lithiation is the opposite. After the half-cell assembly, lithiation occurs first as germanium is not initially lithiated.

Coin-type 2032 half-cells were assembled inside a MBraun glovebox with H_2O and O_2 levels below 0.1 ppm (Fig. 3.2a) according to the scheme showed in Fig. 3.2b. Lithium chips (diameter 15.6 mm x 0.45 mm thickness; MTI Corporations) were employed as reference and counter electrode while dried glass fibers membrane (What-man GF/D) was used as separator. Each coin cell was filled with 200 μL of freshly prepared electrolyte which contains 1 M lithium hexafluorophosphate ($LiPF_6$) dissolved in 1:1 mixture of ethylene carbonate (EC) and dimethyl carbonate (DMC). When expressively mentioned, a certain percentage of additive chosen
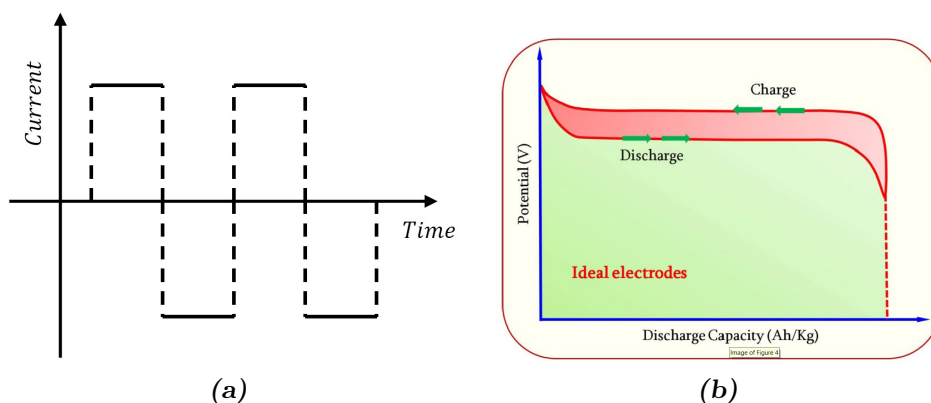
Figure 3.4: *Current profile applied by the galvanostat (a) [84] and galvanostatic lithiation/de-lithiation plot of an ideal electrode (b) [57].*

between vinylene carbonate (VC) or fluoroethylene carbonate (FEC) was added to the electrolyte solution.

Figure 3.3: *BioLogic BCS-805 used to test coin-cells.*

All cells were electrochemically tested in the potential range of 0.01 to 1.5 V using Bio-Logic BCS-805 multichannel battery unit controlled by BT Lab V1.30 (Fig. 3.3). **Galvanostatic voltammetry**, also known as chronopotentiometry, was carried out to assess the cycle ability and the gravimetric capacity of porous germanium electrodes. In this technique, a constant current is applied measuring the voltage response of the cell until it drops to zero. Then, the sign of the constant current is reversed to induce the opposite electrochemical reaction and complete one lithiation/de-lithiation cycle (Fig. 3.4a), repeating this procedure to stress the cell for as many cycles as possible. The charge stored or released by the active material during every half lithiation/de-lithiation cycle, is calculated by the instrument multiplying the

current applied for the time elapsed. The C-rate at which the cell runs is determined by the current applied, which can be properly chosen according to equation 1.6.

In ideal electrodes, lithiation and de-lithiation processes both occur at a constant potential as depicted in Fig. 3.4b, in which the voltage is expressed as a function of gravimetric capacity. The voltage plateau means that only a single process of lithiation or de-lithiation is ideally assumed to happen, i.e. the transition involves only two phases—one lithiated and one not—without any other competing processes in the reaction. The hysteresis is present also when considering

ideal electrodes, due to the polarization arising from the internal resistance of the electrode materials. This polarization decreases the lithiation (discharge) potential below the open circuit voltage, and it increases the de-lithiation (charge) potential to reverse the chemical reaction on the electrode [57]. Here, charge and discharge are mentioned considering the cathodic behaviour of germanium while tested inside half-cells prototypes.

Lithiation/de-lithiation **gravimetric capacity** has been calculated for every half-cycle, dividing the amount of charge flowed by the mass of the active material that has stored or released it. The porous germanium mass for each electrode was evaluated by means of gravimetric measurements, on the basis of the areas involved during the deposition and etching processes (see Fig. 2.7 and Table 2.4). **Coulombic efficiency**, which is defined as the ratio between the charge flowed during the de-lithiation and the one during the lithiation

$$Coulombic\ efficiency\,(\%) = \frac{Q_{de-lithiation}}{Q_{lithiation}} * 100, \tag{3.1}$$

is also calculated. Coulombic efficiency is never 100% because of losses in charge, largely due to secondary reactions or other red-ox reactions in the battery. Nevertheless it is a good parameter to assess the cycle ability and stability of the active material through cycling.

In Fig. 3.5a is reported an example of a galvanostatic plot obtained testing a porous germanium electrode. The curve related to a generic n^{th} cycle is composed by two branches, one corresponding to the lithiation process (red curve) and one to the de-lithiation reaction (blue curve). During lithiation, the voltage decreases until the active material has reached its maximum gravimetric capacity while the amount of charge extracted from the electrode during the de-lithiation is represented as a function of the increasing voltage. In this graph, lithiation and de-lithiation branches are depicted with two different colours to let a better comprehension of which curve is associated to the corresponding reaction. In galvanostatic plots discussed later, lithiation and de-lithiation branches regarding the same cycle will be depicted with the same colour. The two points indicated by the arrows correspond respectively to the lithiation and de-lithiation gravimetric capacity during the nth cycle of that electrode. Collecting these values for each cycle, capacity plots like the one shown in Fig. 3.5b are obtained, from which the lithiation and de-lithiation capacity through cycling is studied. Considering the generic n^{th}-cycle, any difference between the lithiation and de-lithiation capacity implies a coulombic efficiency below 100%, parameter that is also typically reported in capacity plots. Finally, every time lithiation/de-lithiation cycles are performed at different C-rates, it is reported on the graph.

A standard cycling protocol was defined in order to compare electrode performances under the same experimental conditions. The porous Ge compound is not initially lithiated, so the first tenth of cycles were performed at low C-rates
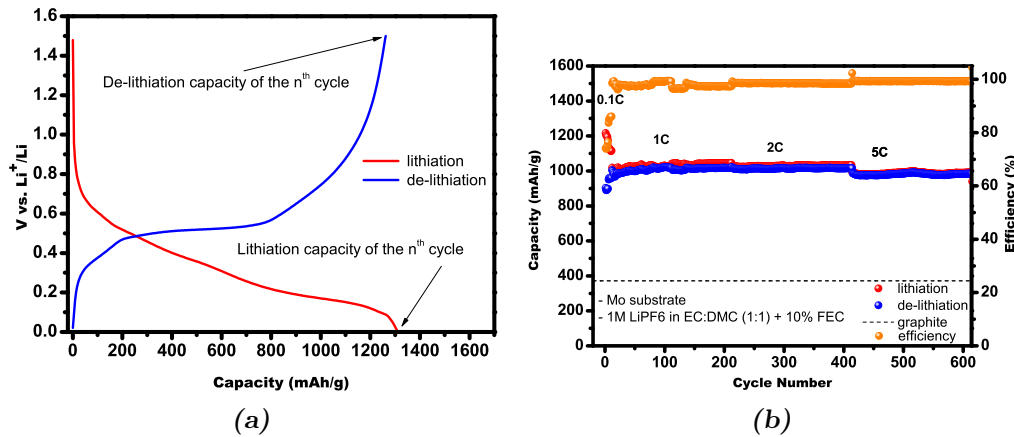
Figure 3.5: *An example of how a galvanostatic (a) and a capacity (b) plot appear.*

(0.1-0.2C), to gradually let Li-ions going into the active material without damaging it and letting the formation of the SEI layer. Then the cells were tested at different C-rates to evaluate the stability and the performances of the porous germanium at different cycling currents. Typically 200 cycles at 1C (one hour lithiation and one hour de-lithiation), 200 cycles at 2C (half an hour each) and 200 cycles at 5C (twelve minutes) were carried out. The current density corresponding to the unit of C-rate was taken as 1C=1600 mA/g, on the basis of the highest germanium gravimetric capacity.

3.2   Results and discussion

In this section, results of galvanostatic voltammetry tests performed on 2032 coin-type half-cells are reported and discussed. Only PECVD-deposited electrodes were tested, as PVD germanium films damaged during the etching procedure (see sect. *2.3*). Gravimetric capacity of lithiation/de-lithiation and coulombic efficiency are plotted in function of the cycle number. Captions of each graphs indicate the main parameters that distinguish the cell in question from the others. Some of them concern the porous germanium electrode—Ge-thickness, metallic substrate, degree of porosity, and active mass— and some others regard the cell-assembly, like the electrolyte additive used. Except for the anode mass loading that is furnished as further detail about the electrode, comparisons are made between prototypes that differ only for one of the parameters listed above, in order to establish how, each of them, influences battery performances. In each graph current C-rates are reported along with the theoretical gravimetric capacity of graphite (372 mAh/g), which represents the threshold value to be overcome in the search of new electrode materials [34].
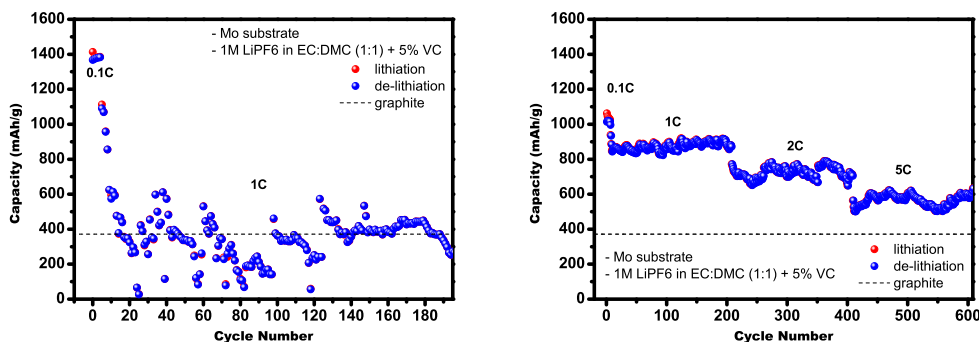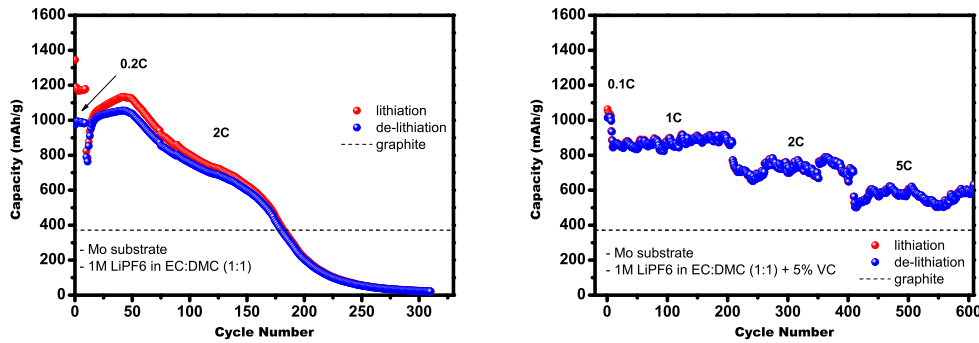
(a) *1 μm-thick bulk Ge@Mo, 5% VC additive, active mass = 1.013 mg.*

(b) *1 μm-thick porous Ge@Mo, etching 1 (40 mA, 180 s), 5% VC additive, active mass = 0.407 mg.*

Figure 3.6: *Lithiation and de-lithiation capacity of a bulk (a) and a porous germanium electrode (b).*

Firstly, the role of the porous structure in improving the cycle life of the electrode is investigated. Fig. 3.6 reports the performances of a bulk germanium electrode vs a nanostructured one. The gravimetric capacity of the 1 μm-thick bulk electrode (Fig. 3.6a) is very unstable and far from the theoretical value of germanium (1624 mAh/g). At a 1C current rate the capacity oscillates around the graphite value before fading, hindering any test at higher C-rates. This trend can be explained through the continuous swelling and cracking of germanium during lithiation and de-lithiation processes, until the complete damaging of the active material. By contrary, the porous structure realized by means of electrochemical etching with HF acid (see sect. *2.5*), reveals to be a solution able to retain 850 mAh/g at 1C and a gravimetric capacity higher than graphite value even at 5C current rate (Fig. 3.6b). Every time the current C-rate is increased, a drop in gravimetric capacity is observed. This capacity drop in increasing the current is typically observed in literature for any kind of active material [5, 47, 51], which can be explained by the fact that it can hardly lithiate completely when the speed of the electrochemical reactions rises. The electrolyte of both cells includes 5% VC additive, whose role is better underlined in the comparison showed in the following figure.

Use of electrolyte additives is an effective method to improve Li-ion battery performances. Helping the formation of a stable SEI layer, enhancing thermal stability of $LiPF_6$ and providing overcharge protection are only some of the many reasons of their effectiveness [32, 86]. The key-role of additive is clearly evidenced in Fig. 3.7. In fact the difference between the capacity plots shown in Fig. 3.7a and Fig. 3.7b can only be attributed to the absence of any additive in the first half-cell and the use of 5% VC in the second one, as the two electrodes are identical. The porous germanium structure assures an initial capacity higher than 800 mAh/g in both cells, which can not be retained when the additive is missing. This underlines the importance of the formation of a stable SEI layer on the surface of the active material to gain a stable capacity through cycling.
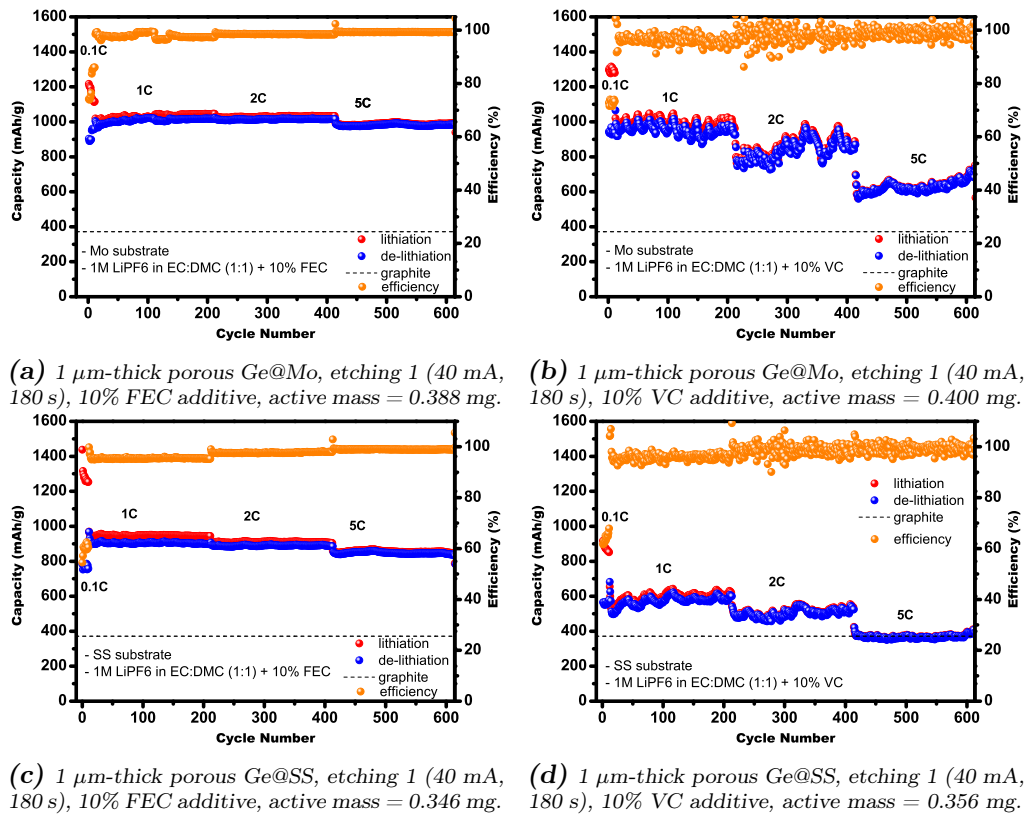
(a) *1 μm-thick porous Ge@Mo, etching 1 (40 mA, 180 s), no additive, active mass = 0.450 mg.*

(b) *1 μm-thick porous Ge@Mo, etching 1 (40 mA, 180 s), 5% VC additive, active mass = 0.407 mg.*

Figure 3.7: *Capacity plots of two identical electrodes assembled in half-cells without (a) and with (b) additive.*

The role of electrolyte additives is deeply investigated through comparisons showed in Fig. 3.8, which regard half-cells using vinylene carbonate (VC) and fluoroethylene carbonate (FEC). These are the most common electrolyte additives used to improve the stability of SEI in Si, Ge and Sn based anode materials [26,32]. Fig. 3.8a and Fig. 3.8b are the capacity plots of 1 μm-thick porous germanium electrodes deposited on molybdenum substrate assembled in half-cells with FEC and VC additive respectively. After some initial cycles at 0.1C, both cells were stressed through more than 600 cycles at different C-rates showing a remarkable 1000 mAh/g capacity at 1C. The same cycling protocol was applied to a couple of prototypes containing electrodes deposited on stainless steel making use of FEC (Fig. 3.8c) and VC (Fig. 3.8d) additives. Comparing capacity plots of electrodes deposited on the same substrate (Fig. 3.8a-3.8b or Fig. 3.8c-3.8d) it can be stated that FEC additive plays a significant role in retaining a more stable and higher capacity with respect to VC-cells. The major difference can be noticed at higher C-rates. In fact, despite both Mo-substrate electrodes show a capacity of nearly 1000 mAh/g at 1C, at 5C current rate the capacity of the FEC-cell is still around 900 mAh/g while the one of VC-cell drops at nearly 600 mAh/g. FEC is known to facilitate the formation of mechanically stable solid electrolyte interface (SEI) which acts as a passivating layer to inhibit further electrolyte reduction that cause capacity fading [32,86]. Comparing graphs of FEC-cells (Fig. 3.8a-3.8c) and VC-cells (Fig. 3.8b-3.8d) separately, emerges a superior gravimetric capacity shown from Mo-substrate electrodes. This difference is more evident looking at VC-cells (Fig. 3.8b-3.8d) because at 1C current rate the Mo-electrode has nearly 1000 mAh/g capacity while the SS-one reaches only 600 mAh/g. One hypothesis could be that molybdenum is playing an active role inside the cell, as compounds containing MoO_3 are included among anodic active materials. Another possible explanations is related to the different conductivities of the two metals, being $18.7*10^6$ S/m for molybdenum [87] and $1.32*10^6$ S/m for stainless steel [88]. The charge transfer occurring at the junction between conductive substrate and active

(a) *1 μm-thick porous Ge@Mo, etching 1 (40 mA, 180 s), 10% FEC additive, active mass = 0.388 mg.*

(b) *1 μm-thick porous Ge@Mo, etching 1 (40 mA, 180 s), 10% VC additive, active mass = 0.400 mg.*

(c) *1 μm-thick porous Ge@SS, etching 1 (40 mA, 180 s), 10% FEC additive, active mass = 0.346 mg.*

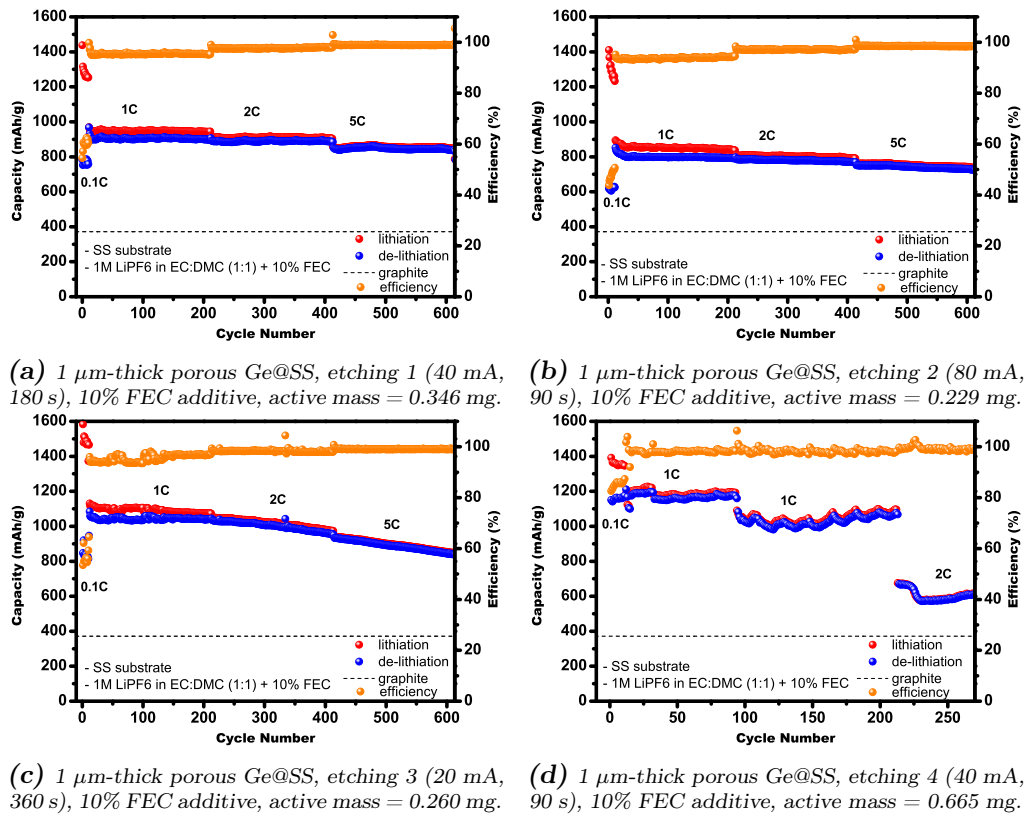**(d)** *1 μm-thick porous Ge@SS, etching 1 (40 mA, 180 s), 10% VC additive, active mass = 0.356 mg.*

Figure 3.8: *Comparison between 1 μm-thick porous germanium anodes deposited on molybdenum (a-b) or stainless steel substrate (c-d) and assembled in half-cells with FEC (a-c) or VC (b-d) additive.*

material, depends on the conductivity of both materials. Molybdenum, having a higher conductivity, provides an ease in charge transfer allowing more lithiation and de-lithiation, consequently giving more capacity. Nevertheless this point needs further investigations to be deeply explained.
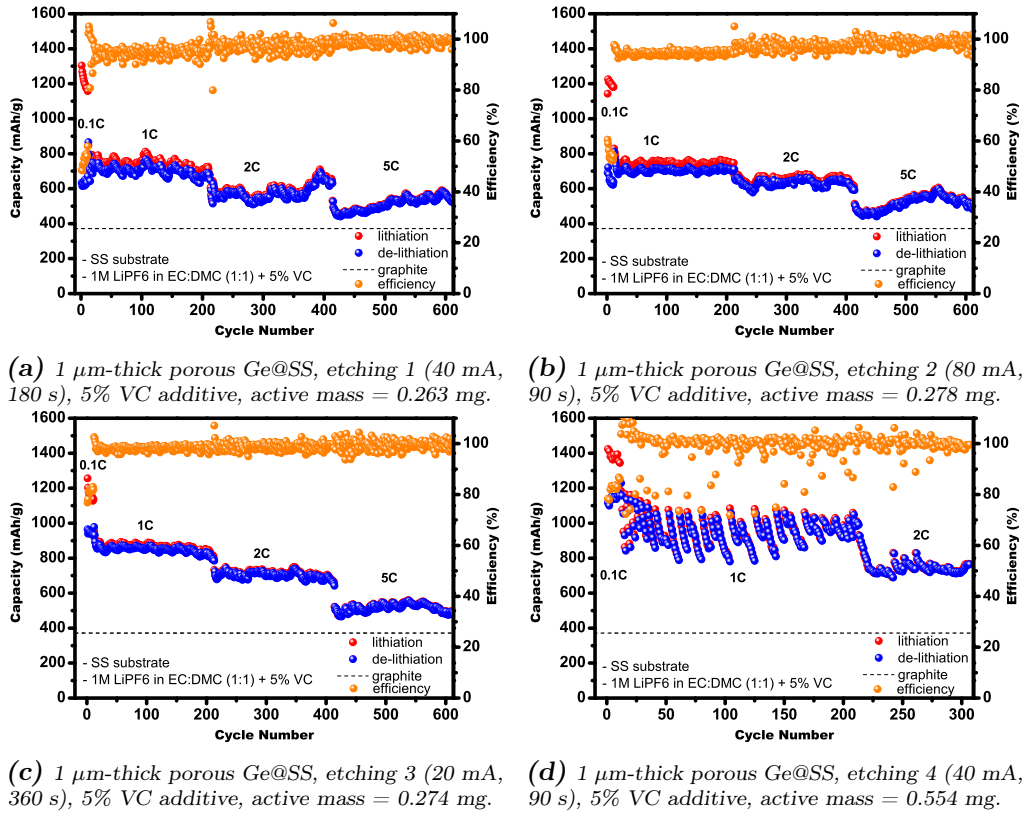
The porous nanostructure of the germanium active material plays a fundamental role in increasing the cycle ability of the cell [34], as already underlined through the comparison reported in Fig. 3.6. Electrodes on stainless steel substrates with different degree of porosity were realized (see sect. *2.5*) in order to investigate any relation between electrochemical performances and the structures obtained through each etching recipes reported in Table 2.7. Capacity plots regarding electrodes fabricated with all four etching recipes are reported both in Fig. 3.9 and in Fig. 3.10. The first figure regards FEC-cells while the second is composed by VC-cell graphs and, as already discussed, FEC additive helps stabilizing and increasing the capacity through cycling, whatever is the nanostructure considered. More than 600 cycles at 1,2, and 5 C-rates were performed on all cells. No clear advantage can be seen in etching 1 (Fig. 3.9a, 3.10a) rather than etching 2 (Fig. 3.9b, 3.10b) samples. The capacity values of VC-cells are nearly the same (Fig. 3.10a-3.10b), while etching 1-sample shows a slightly higher performance than etching 2-sample in FEC-cells. These are expected results as any substantial difference was noticed between the morphologies of etching 1 and etching 2 samples (Fig. 2.16a-2.16b). Etching 3-samples show a more rapid capacity decay with both additives (Fig. 3.9c, 3.10c) with respect to etching 1 and 2 samples. This is probably due to wider Ge-pillars created by etching 3 (Fig. 2.16c) in comparison with the first two recipes. Larger Ge-structures may suffer from a faster degradation due to the volume expansion induced by lithiation and de-lithiation processes, causing a more pronounced capacity fading. Etching 4 samples (Fig. 3.9d, 3.10d) deserve a separate discussion. As already mentioned in sec. *2.5*, this etching recipe removed only half of Ge-mass with respect to recipes 1-3. Fig. 2.17d clearly shows that only the upper part of the Ge-film is porous while the lower half is still bulk. The oscillating behavior of the capacity in Fig. 3.10d resembles the one showed by the bulk sample in Fig. 3.6a, testifying that part of this anode is still behaving like bulk germanium, while the quite higher capacity value—around 1000 mAh/g—is due to the porous part of it. The capacity of etching 4-sample in FEC-cell halves when doubling the C-rate (Fig. 3.9d), as nanostructuring only half of germanium films is not enough to retain capacity when the current rate is increased. None of the two etching 4-samples could withstand current rate higher than 2C, as the partially bulk active material degraded.

1 μm-thick porous samples have 0.3-0.4 mg of active mass on average, corresponding to densities of 0.17-0.22 mg/cm^2. To approach densities of active mass per unit of electrode area found in literature (0.5-1 mg/cm^2 [5,51]), thicker PECVD Ge-films were deposited and tested in half-cells. 5 μm thickness has been chosen to reach an areal density of 0.8 mg/cm^2. Fig. 3.11 reports a comparison

(a) *1 µm-thick porous Ge@SS, etching 1 (40 mA, 180 s), 10% FEC additive, active mass = 0.346 mg.*

(b) *1 µm-thick porous Ge@SS, etching 2 (80 mA, 90 s), 10% FEC additive, active mass = 0.229 mg.*

(c) *1 µm-thick porous Ge@SS, etching 3 (20 mA, 360 s), 10% FEC additive, active mass = 0.260 mg.*

(d) *1 µm-thick porous Ge@SS, etching 4 (40 mA, 90 s), 10% FEC additive, active mass = 0.665 mg.*

Figure 3.9: *Comparison between 1 µm-thick porous germanium anodes deposited on stainless steel substrate and assembled in half-cells with FEC additive.*

(a) *1 µm-thick porous Ge@SS, etching 1 (40 mA, 180 s), 5% VC additive, active mass = 0.263 mg.*

(b) *1 µm-thick porous Ge@SS, etching 2 (80 mA, 90 s), 5% VC additive, active mass = 0.278 mg.*

(c) *1 µm-thick porous Ge@SS, etching 3 (20 mA, 360 s), 5% VC additive, active mass = 0.274 mg.*

(d) *1 µm-thick porous Ge@SS, etching 4 (40 mA, 90 s), 5% VC additive, active mass = 0.554 mg.*
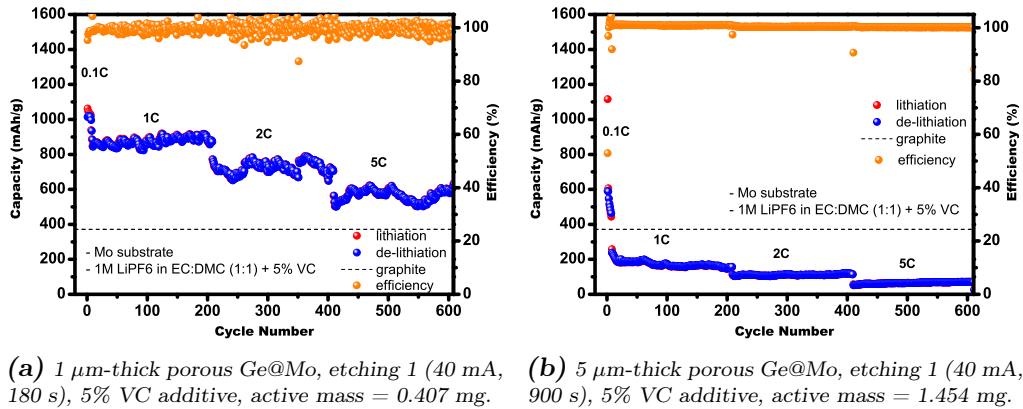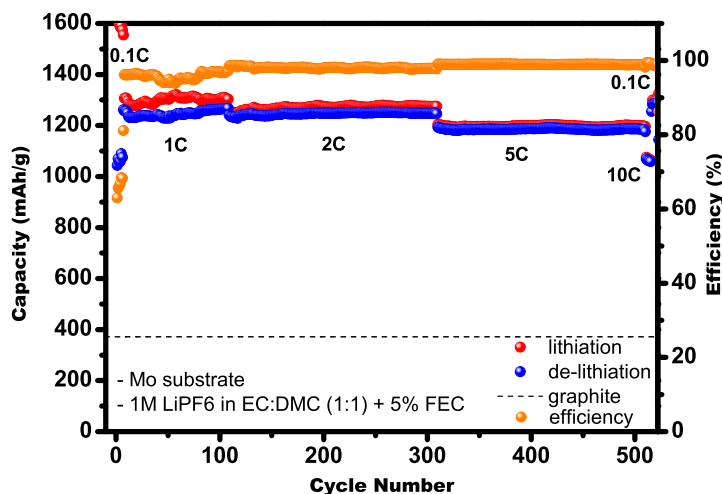
Figure 3.10: *Comparison between 1 µm-thick porous germanium anodes deposited on stainless steel substrate and assembled in half-cells with VC additive.*

(a) *1 µm-thick porous Ge@Mo, etching 1 (40 mA, 180 s), 5% VC additive, active mass = 0.407 mg.*

(b) *5 µm-thick porous Ge@Mo, etching 1 (40 mA, 900 s), 5% VC additive, active mass = 1.454 mg.*

Figure 3.11: *Comparison between 1 µm-thick (a) and 5 µm-thick (b) porous germanium anodes deposited on molybdenum substrate and assembled in half-cells with VC additive.*

between thin and thick Ge-electrodes assembled in half-cells with VC additive and cycled for more than 600 cycles at 1,2, and 5C current rate. The performances showed by the thicker electrode are not satisfactory, as the capacity is even lower than the theoretical graphite value at any C-rate, except for initial cycles at 0.1C. Nevertheless it is worth to note that although the capacity is low, it is stable through cycling, suggesting that probably only a small part of germanium is actually taking part to lithiation/de-lithiation processes. The fact that only a small fraction of germanium actively participates in the reaction, does not affect the overall stability of the electrode, which is comparable to the thinner one (Fig. 3.11a) and shows a coulombic efficiency of nearly 100%. The porous structure of thicker Ge-films presents larger pillars with respect to the pore-morphology of thin films (Fig. 2.20), and probably only the superficial Ge is working as Li-ions cannot penetrate into the core of Ge-structures. Post-mortem analysis are required to investigate this issue and, if this hypothesis will be confirmed, a proper etching recipe to realize a finer porosity also in thicker Ge-films is needed, in order to exploit all the germanium available on the electrode.

The experience gained through this thesis work, led to the result shown in Fig. 3.12, which are the best performances achieved so far. It refers to a 1 μm-thick Ge-layer on molybdenum substrate, nanostructured with etching recipe number 1 and assembled in a half-cell with FEC additive. The tests performed on this cell—named G51—, aimed to stress it at high current rates for as many cycles as possible. This is the reason why, after some initial cycles at 0.1C, only 100 cycles at 1C were carried out instead of the usual 200 cycles. Then, the usual protocol continued—200 cycles at both 2C and 5C— before performing some cycles at 10C, which exhibited an astonishing 1050 mAh/g capacity. After that, the C-rate was re-established to 0.1C, to assess whether the active material could re-gain the initial capacity or not. A comparison between 0.1C performances is reported


Figure 3.12: *G51-cell: 1 μm-thick porous Ge@Mo, etching 1 (40 mA, 180 s), 5% FEC additive, active mass = 0.244 mg.*
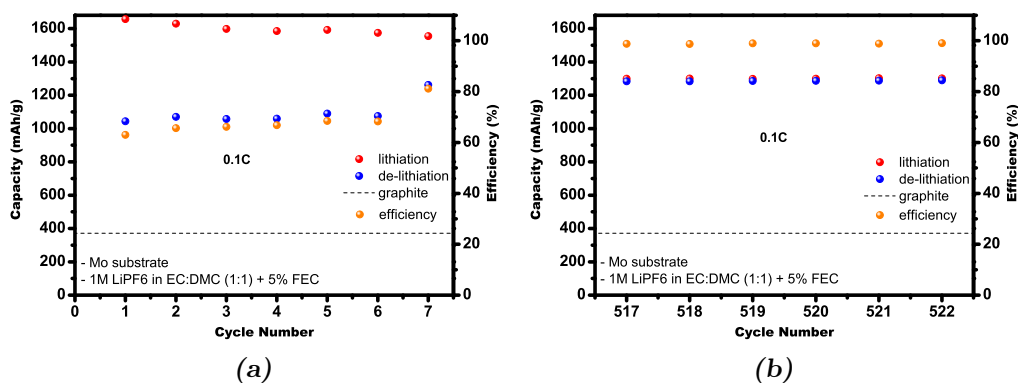
Figure 3.13: *G51-cell: comparison between cycles performed at 0.1C rate.*

in Fig. 3.13. A very low efficiency is measured in the first tenth of cycles (Fig. 3.13a), owing to a large irreversible capacity occurring during the formation of the SEI layer and parasitic reactions inside the cell, not present in Fig. 3.13b. After more than 500 cycles, the porous germanium active material was still performing a gravimetric capacity higher than 1300 mAh/g at 0.1C, and no more irreversible capacity was detected as the coulombic efficiency was approaching 100%. This represents a clear evidence of the high stability of the porous Ge-active material that encouraged further cycling tests at 5C current rate. Fig. 3.14 reports the capacity plot of G51-cell extended to 1000 cycles, whose gravimetric capacity was still above 1100 mAh/g after further 500 cycles at 5C. This value corresponds to 70% of the theoretical capacity of germanium and a storage capability three times better than the theoretical value of graphite.
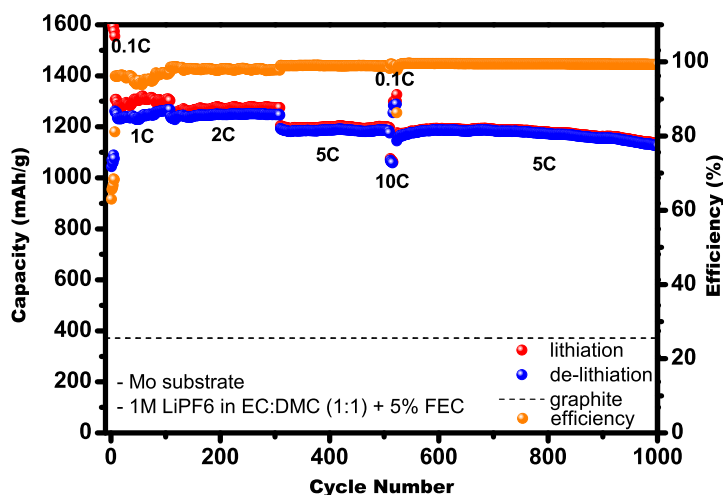
Figure 3.14: *G51-cell: capacity plot extended to 1000 cycles.*

Galvanostatic plots concerning the sample G51, can give further details regarding the stability of this Ge-based active material. Fig. 3.15 reports a comparison

between the first two cycles performed at 0.1C rate. In the voltage range 0.3-1.1 V, the lithiation branch of the first cycle is quite different with respect to the second. This slope variation is ascribed to the formation of SEI layer on the active material, as commonly reported in literature [32, 44]. Below 0.3 V the two curves coincide reaching a gravimetric capacity close to the highest theoretical value of germanium (1624 mAh/g). This multiple plateau behavior is indicative of lithium insertion into equipotential sites and suggests that various Li-Ge phases are forming during the electrochemical lithiation/de-lithiation [36, 44]. The absence of
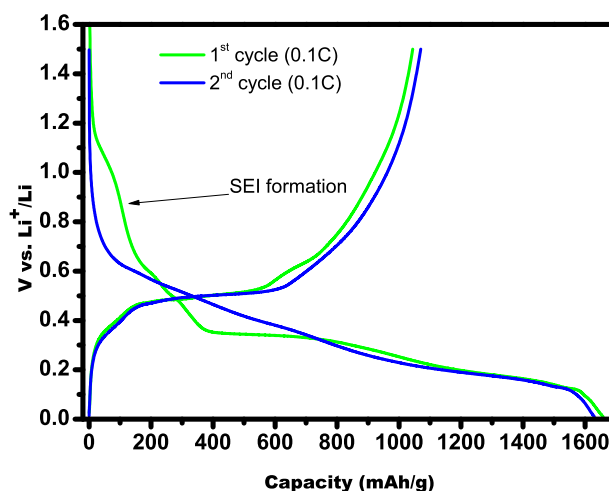

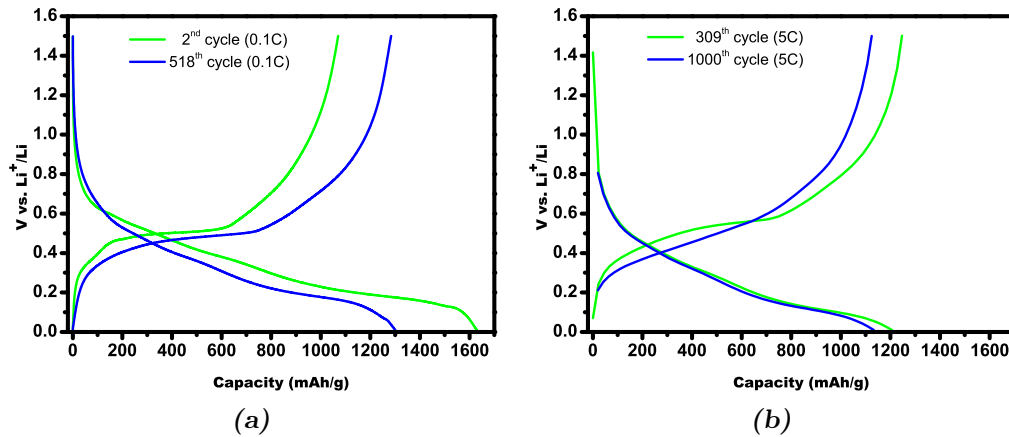**Figure 3.15:** *G51-cell: galvanostatic plots of the first two cycles.*

the reduction plateau around 0.8 V in the second lithiation cycle, indicates that the SEI formation is suppressed, as a good and stable one is already formed. A shift of lithium insertion potentials towards more positive value was observed during the second cycle, which could be due to the conversion of poly-crystalline germanium into amorphous one, occurred during the first cycle and SEI formation [44, 45]. Nevertheless, in both cycles is detected a great irreversible capacity, as only part of the charge stored during the lithiation can be extracted from the active material during the de-lithiation, owing to parasitic reaction inside the cell.

This sample showed great capability retention at any C-rates. Fig. 3.16a shows a comparison between the already discussed 2nd cycle and another one performed at 0.1C. In the 518th cycle curve, the irreversible capacity is disappeared and an impressively reversible capacity of 1300 mAh/g is measured. Even at 5C current rate the coulombic efficiency is nearly 100% and the capacity is above 1100 mAh/g in both cases (Fig. 3.16b). A minimal loss of capacity is detected, mainly due to the normal degradation of the active material occurred during the 700 cycles that separate this two measures.

Graphs concerning galvanostatic measurements performed at all the considered C-rates, are superimposed in Fig. 3.17. Increasing the C-rate, both lithiation and de-lithiation branches become steeper, as the gravimetric capacity diminishes. This

(a) (b)

Figure 3.16: *G51-cell: comparison between galvanostatic plots concerning cycles performed at 0.1C (a) and 5C (b).*

is due to the fact that increasing the current, not all the active material is able to store and release Li-ions. Nevertheless, at any C-rate the capacity measured during lithiation nearly equals the one during the de-lithiation, implying a coulombic efficiency around 100% and a high reversibility of the whole process involved.
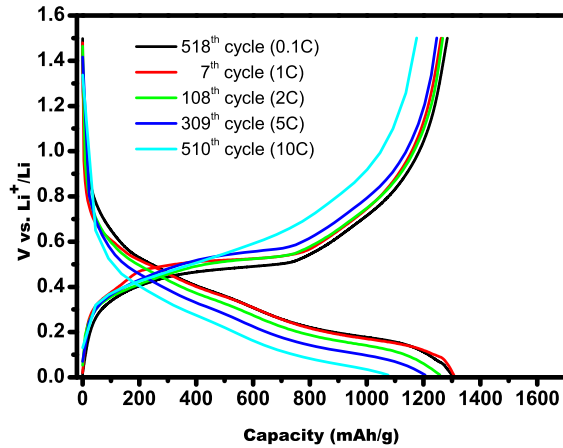
Figure 3.17: *G51-cell: superimposition of galvanostatic plots performed at all the considered C-rates.*

Going beyond 1000 cycles of lithiation/de-lithiation and achieving stable capacity and coulombic efficiency at C-rates up to 5C, make this Ge-based electrode among the best candidates to replace commercial graphite-ones in future high energy density lithium-ion batteries.

Further steps are needed to bring this technology from a research area to an industrial one. Performances achieved by 1 μm-thick samples should be confirmed also for anodes with increased active mass for electrode area, around 1 mg/cm^2 [5, 51]. Subsequently, a detailed study about realizing full cells with this anode is fundamental to evaluate the proper choice of cathode and electrolyte, in order

to exploit the capacity of these Ge-based anodes that is three times higher than graphite. Finally, laboratory equipments for the PECVD-deposition and for the electrochemical etching must be scaled up for industrial mass production. However these techniques are already employed in industrial processes, since both PECVD and wet etching are widely used in semiconductor tools fabrication.

Conclusions and further works

This thesis work concerned the development of a binder-free nanoporous germanium anode for lithium-ion batteries.

Germanium films were deposited by means of PECVD (Plasma Enhanced Chemical Vapour Deposition) on metallic substrates acting as current collectors. Neither of the two metallic substrates—molybdenum and stainless steel—needed any binder or adhesion layer to prevent the detachment of the germanium active material from them. This is an advantage with respect to typical anodes in which binders are used to conglomerate the active material making it adhere to the substrate, causing an increase in weight without contributing to the energy storage of the device. Furthermore, germanium has a theoretical gravimetric capacity of 1600 mAh/g, four times higher than graphite (372 mAh/g), which is the most diffused anode material in commercial devices. Nevertheless, to exploit germanium as negative electrode in Li-ion batteries a nanostructure must be created, as bulk semiconductor can not withstand the huge volume expansion occurring during lithiation and de-lithiation cycles. The porous structure created by means of an electrochemical etching with hydrofluoric acid revealed to be effective in creating a compliant matrix able to guarantee a stable cycle ability of the electrode.

Within this thesis work, a process for the PECVD deposition and one for the nanostructuration of germanium films were implemented. Furthermore, was established a partnership with the Italian Institute of Technology (IIT) of Genoa and the Bruno Kessler Foundation (FBK) of Trento to perform all the characterizations required.

More than 1000 lithiation and de-lithiation cycles at different C-rates up to 5C were carried out retaining a capacity above 1100 mAh/g, three times higher than the theoretical graphite value. These results—presented at the 69th meeting of the International Society of Electrochemistry (ISE-2018)—were obtained testing electrodes in coin-type 2032 half-cells using metallic lithium as counter electrode. Many are the solutions adopted to fabricate different type of electrodes, varying the metallic substrate—molybdenum or stainless steel—the porous morphology, the germanium thickness and the electrolyte additive. The best results were shown

by a 1 μm-thick porous Ge-layer deposited on molybdenum substrate making use of fluoroethylene carbonate (FEC) as additive to stabilize and improve the active material capacity.

Physical Vapor Deposition (PVD) was investigated as alternative technique to deposit germanium, but adhesion problems hindered any electrochemical test of PVD-deposited electrodes. Deeper investigations are needed to overcome adhesion issues and to exploit also PVD for the fabrication of porous germanium electrodes.

This work confirms that germanium-based electrode are among the best candidates to replace commercial graphite-ones in future high energy density lithium-ion batteries. A patent regarding the process presented in this thesis to realize porous germanium anodes for LIBs has been already filed (IT 102018000006103).

Within the ANGELS project funded by ASI (Italian Space Agency), the DIEE-Department of the University of Cagliari will develop electric models to be used for the design of a BMS (Battery Management System) concerning cells assembled with the anode presented in this thesis work.

Further works will regard developing anodes with increased areal density of active mass that could attain the same performances showed by 1 μm-thick Ge-anodes. Furthermore full cells with this anodes should be realized, evaluating which are the best electrolyte solutions and cathode materials to fully exploit the high gravimetric capacity of porous germanium anodes. Finally the high cost of germanium as raw material requires a proper choice of the application fields for this technology—like space or medical applications—scaling up the laboratory equipments for industrial processes.

# Appendices

A

SIMS: Secondary Ion Mass Spectrometry

During this thesis work, compositional sample analysis were carried out by secondary ion mass spectrometry (SIMS). In this appendix basic principles and the main components of a SIMS equipment are treated.

1.1 Basic principles

Among the commonly used surface analytical techniques, secondary ion mass spectrometry (SIMS) is one of the most sensitive. Even very low concentrations of trace elements, such as those used intentionally as dopants and impurities, can be detected. Concentration as low as part per million (ppm) and in some cases part per billion (ppb) can be measured, providing elemental depth profiles over a depth range from a few angstroms to tens of micrometers. SIMS can be used for both elemental surveys and isotopic analysis of small samples, even particles [89]. The high sensitivity allows a high dynamic range, typically over 6 orders of magnitude, enabling depth profiling for both high and low element concentrations and monitor thin film composition, stacks and interfaces.

During SIMS analysis a sample is introduced in a ultra-high vacuum (UHV) chamber (10^{-7}-10^{-9} mbar) and bombarded with a finely focused beam of primary ions—e.g. O_2^+, O^+, Cs^+, or Ga^+—with an average energy between 0.5 and 25 keV to induce sputtering. The incident ions are implanted into the sample surface with a penetration depth up to 10 nm, depending on the primary beam energy. During the collision cascade, some atoms/clusters of atoms of the sample can acquire a momentum with direction toward the sample surface. If their kinetic energy is higher than the surface binding energy, they will be ejected into the vacuum chamber giving place to the effect of sputtering, which results in the progressive

erosion of the surface. The schematic representation of the described process is shown in Fig. A.1.
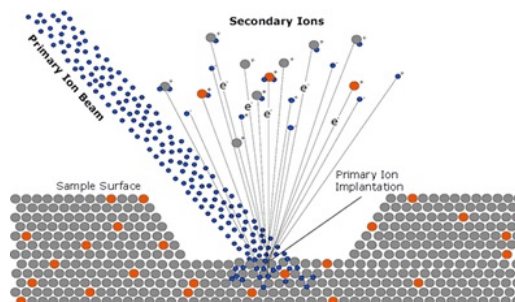
Figure A.1: *Schematic representation of the sputtering process occurring during SIMS analysis [90].*

The secondary ion yields will vary greatly according to the chemical environment of the sample and the sputtering conditions (primary ion, energy of the beam, incidence angle). The particles eroded by the primary ion beam are usually emitted with a low kinetic energy (5 - 10 eV), and more than 95% of them come from the top 2 monolayers of the sample. The sputtered particles are atoms and molecules most of which are neutral. Nevertheless, in optimal conditions about 1 - 5% of these particles are ionized and can be collected and analyzed using a mass spectrometer [91].

During SIMS analysis both negative and positive ions are emitted as single particles and clusters. In order to enhance the sensitivity for ionized particles in either ways, SIMS instruments are equipped with sources able to increase ionization efficiency of both positive and negative ions. When oxygen is employed as primary ion, it causes partial or total oxidation of the bombarded surfaces, generating the formation of surface enhancing and then the emission of positive secondary ions, particularly for electropositive elements. If the sample is bombarded with cesium, the increase of Cs concentration on the surface modifies the work function of the material, favoring the passage of electrons by tunnel effect from the surface to the emitted ions. The net effect is an enhancement of negative secondary ions, particularly for electronegative species [92].

Many are the advantages of SIMS technique, beside the already mentioned sensitivity. Almost all the elements can be detected, isotopic species can be discriminated and also insulators can be analyzed. Furthermore, a few nanometers depth resolution can be reached and chemical information can be obtained from detected molecular ions. To carry out quantitative analysis the presence of adequate standards is required, representing an advantage or a drawback depending on whether a reference sample is available or not. The main disadvantages of SIMS are that is a destructive analysis, the ion emission strongly depends on the matrix and flat surfaces are required in order to reach high depth resolution.

1.2 SIMS equipment

Depending on the flux of primary ions two SIMS configurations can be defined, static and dynamic SIMS. In static SIMS, particularly indicated for surface analysis and ion mapping, the current density of the primary ion beam is low ($< 10 \, \text{nA/cm}^2$), corresponding to an extremely low sputtering rate $\sim 0.1 \, \text{nm/h}$. In dynamic SIMS, which is more specific for bulk analysis and elemental depth profiling, the primary beam density is set at higher values ($3 \, \mu\text{A/cm}^2$-$1 \, \text{mA/cm}^2$), resulting in higher sputtering rates ($\geq 1 \, \text{nm/s}$) allowing depth profiling of the bombarded material. A schematic representation of dynamic SIMS instrument is shown in Fig. A.2.
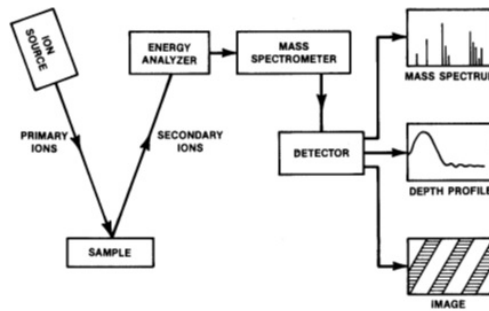
Figure A.2: *Schematic representation of dynamic SIMS instrument [93].*

One of the main constituents is the ion source species, which is established depending on the required current, beam dimension, and the composition of the sample to be analyzed. Into the primary ion gun, primary beam is focalized and oriented through lenses. The extraction column contains the extraction lenses and focalization systems close to the mass analyzer, which is a sector field mass spectrometer that uses a combination of an electrostatic and a magnetic analyzer to separate the secondary ions according to their mass and charge. Finally, a detector counts the number of ions of the secondary beam in function of their mass and charge [82].

Figure A.3: *SIMS Cameca SC Ultra/Wf, present at Bruno Kessler Foundation laboratories.*

In this work, SIMS analyses were performed using a Cameca SC Ultra/Wf

instrument (Fig. A.3) with a magnetic sector analyzer. This instrument is optimized to perform analyses with ultra-low impact energy ($\leq$ 1keV) and it is equipped with an O_2^+ and Cs^+ ion sources. The primary beam incidence angle is fixed at 60° with respect to the sample normal.

Bibliography

[1] J. Ocon, J. Lee and J. Lee, 25 (2014).

[2] G. Berckmans et al., Energies 10 (2017).

[3] Y. Liu, S. Zhang and T. Zhu, ChemElectroChem 1 (2014) 706.

[4] N.G. Rudawski et al., Applied Physics Letters 100 (2012) 083111, https://doi.org/10.1063/1.3689781.

[5] A.M. Chockla et al., ACS Applied Materials & Interfaces 4 (2012) 4658, https://doi.org/10.1021/am3010253, PMID: 22894797.

[6] M. Ge et al., Nano Letters 14 (2014) 261, https://doi.org/10.1021/nl403923s, PMID: 24279924.

[7] S. Goriparti et al., Journal of Power Sources 257 (2014) 421 .

[8] D. Li et al., JOURNAL OF MATERIALS CHEMISTRY A 1 (2013) 14115.

[9] C. Botas et al., ACS Applied Materials & Interfaces 8 (2016) 28800, https://doi.org/10.1021/acsami.6b07910, PMID: 27709889.

[10] D. Cho et al., Nanoscale Research Letters 10 (2015) 424.

[11] T. Kennedy et al., Nano Letters 14 (2014) 716, https://doi.org/10.1021/nl403979s, PMID: 24417719.

[12] D. Wang et al., Journal of the American Chemical Society 126 (2004) 11602, https://doi.org/10.1021/ja047435x, PMID: 15366907.

[13] J. Graetz et al., Journal of The Electrochemical Society 151 (2004) A698, http://jes.ecsdl.org/content/151/5/A698.full.pdf+html.

[14] C.S. Fuller and J.A. Ditzenberger, Phys. Rev. 91 (1953) 193.

[15] C.S. Fuller and J.C. Severiens, Phys. Rev. 96 (1954) 21.

[16] N. Nitta et al., Materials Today 18 (2015) 252 .

[17] A.J. McEvoy, EPJ Web of Conferences 54 (2013) 01018.

[18] B. Scrosati, Journal of Solid State Electrochemistry 15 (2011) 1623.

[19] B. Scrosati, Lithium Batteries: from early stages to the future (Wiley-Blackwell, 2013) chap. 2, pp. 21–38, https://onlinelibrary.wiley.com/doi/pdf/10.1002/9781118615515.ch2.

[20] D. Linden and T. Reddy, Handbook of batteries (McGraw-Hill, 2002).

[21] T. Reddy, Linden's Handbook of Batteries, 4th Edition (McGraw-Hill Education, 2010).

[22] A. Wang et al., npj Computational Materials 4 (2018) 15.

[23] M. Winter, Zeitschrift Fur Physikalische Chemie-international Journal of Research in Physical Chemistry & Chemical Physics - Z PHYS CHEM 223 (2009) 1395.

[24] S.J. An et al., Carbon 105 (2016) 52 .

[25] J.B. Goodenough, H.D. Abruna and M.V. Buchanan.

[26] A.L. Michan et al., Chemistry of Materials 28 (2016) 8149, https://doi.org/10.1021/acs.chemmater.6b02282.

[27] C. Julien et al., Lithium Batteries (Springer International Publishing, Cham, 2016) pp. 29–68.

[28] M.B. Armand, Intercalation Electrodes (Springer US, Boston, MA, 1980) pp. 145–161.

[29] M. Lazzari and B. Scrosati, Journal of The Electrochemical Society 127 (1980) 773, http://jes.ecsdl.org/content/127/3/773.full.pdf+html.

[30] G.L. Xu et al., J. Mater. Chem. A 2 (2014) 19941.

[31] C. Julien et al., Basic Elements for Energy Storage and Conversion (Springer International Publishing, Cham, 2016) pp. 1–27.

[32] U. Gulzar et al., Electrochimica Acta (2018).

[33] M.H. Park et al., Nano Letters 9 (2009) 3844, https://doi.org/10.1021/nl902058c, PMID: 19746961.

[34] C. Julien et al., Anodes for Li-Ion Batteries (Springer International Publishing, Cham, 2016) pp. 323–429.

[35] S. Goriparti et al., ACS Applied Materials & Interfaces 7 (2015) 25139, https://doi.org/10.1021/acsami.5b06426, PMID: 26492841.

[36] C. Zhong et al., J. Mater. Chem. A 1 (2013) 10798.

[37] I.S. Hwang et al., Chem. Commun. 48 (2012) 7061.

[38] CN105070891 (2015).

[39] CN105529442 (2016).

[40] CN106099066 (2016).

[41] C.M. Park et al., Chem. Soc. Rev. 39 (2010) 3115.

[42] S. Yoon, C.M. Park and H.J. Sohn, Electrochemical and Solid-State Letters 11 (2008) A42, http://esl.ecsdl.org/content/11/4/A42.full.pdf+html.

[43] L. Baggetto and P.H. Notten, Journal of The Electrochemical Society 156 (2009) A169, http://jes.ecsdl.org/content/156/3/A169.full.pdf+html.

[44] H. Jung et al., Chemistry of Materials 27 (2015) 1031, https://doi.org/10.1021/cm504312x.

[45] L.Y. Lim et al., Chemistry of Materials 26 (2014) 3739, https://doi.org/10.1021/cm501233k.

[46] G. Goward et al., Journal of Alloys and Compounds 329 (2001) 82 .

[47] L.Y. Lim et al., Advanced Energy Materials 5 (2015) 1500599, https://onlinelibrary.wiley.com/doi/pdf/10.1002/aenm.201500599.

[48] H. Gao et al., Nano Letters 17 (2017) 1512, https://doi.org/10.1021/acs.nanolett.6b04551, PMID: 28177638.

[49] M. Haro et al., Phys. Chem. Chem. Phys. 16 (2014) 17930.

[50] B. Laforge et al., Journal of The Electrochemical Society 155 (2008) A181, http://jes.ecsdl.org/content/155/2/A181.full.pdf+html.

[51] D.T. Ngo et al., Energy Environ. Sci. 8 (2015) 3577.

[52] US2017033356A1 (2016).

[53] US2016043385A1 (2016).

[54] US9368836 (B2) (2015).

[55] CN106159247 (2016).

[56] CN103943836 (2014).

[57] C. Liu, Z.G. Neale and G. Cao, Materials Today 19 (2016) 109 .

[58] K. Mizushima et al., Materials Research Bulletin 15 (1980) 783 .

[59] K. Mizushima et al., Solid State Ionics 3-4 (1981) 171 .

[60] B. Scrosati and J. Garche, Journal of Power Sources 195 (2010) 2419 .

[61] T. Ohzuku and Y. Makimura, Chemistry Letters 30 (2001) 642, https://doi.org/10.1246/cl.2001.642.

[62] C. Julien et al., Cathode Materials with Two-Dimensional Structure (Springer International Publishing, Cham, 2016) pp. 119–162.

[63] M.M. Thackeray, Materials Research Bulletin 18 (1983) 461 .

[64] M.M. Thackeray, Journal of The Electrochemical Society 142 (1995) 2558, http://jes.ecsdl.org/content/142/8/2558.full.pdf+html.

[65] C. Julien et al., Cathode Materials with Monoatomic Ions in a Three-Dimensional Framework (Springer International Publishing, Cham, 2016) pp. 163–199.

[66] A.K. Padhi, K.S. Nanjundaswamy and J.B. Goodenough, Journal of The Electrochemical Society 144 (1997) 1188, http://jes.ecsdl.org/content/144/4/1188.full.pdf+html.

[67] M. Park et al., Angewandte Chemie International Edition 50 (2011) 9647.

[68] F.W. Yuan, H.J. Yang and H.Y. Tuan, ACS Nano 6 (2012) 9932, https://doi.org/10.1021/nn303519g, PMID: 23043347.

[69] S. Choi et al., Small 13 (2017).

[70] T. Ormston et al., SpaceOps Conferences (American Institute of Aeronautics and Astronautics, 2014) chap. Lithium Ion Battery Management Strategies for European Space Operations Centre Missions.

[71] http://www.esa.int/esapub/bulletin/bulletin129/bul129f_teston.pdf.

[72] A. Kumar and K. Mueller, AIAA SPACE Forum (American Institute of Aeronautics and Astronautics, 2015) chap. Operational Experience with Nickel Hydrogen and Lithium Ion Batteries.

[73] https://www.nasa.gov/directorates/heo/scan/definitions/glossary/index.html.

[74] https://www.nasaspaceflight.com/2017/01/spacewalkers-upgrading-iss-batteries/.

[75] N. Williard et al., Energies 6 (2013) 4682.

[76] https://ntrs.nasa.gov/archive/nasa/casi.ntrs.nasa.gov/20100028067.pdf.

[77] R. Marsh et al., Journal of Power Sources 97-98 (2001) 25 , Proceedings of the 10th International Meeting on Lithium Batteries.

[78] Saft batteries...powering outer space for 50 years , https://www.saftbatteries.com/.

[79] P. Walker, Handbook of Metal Etchants (CRC Press, 1990).

[80] M. Meyyappan et al., Plasma Sources Science and Technology 12 (2003) 205.

[81] G. Calabrese, Relaxed germanium epilayers on porous silicon buffers for low dislocation content Ge on Si virtual substrates, PhD Thesis, University of Ferrara (2014).

[82] M. Boschetti, PECVD growth of Ge for nanoporous lithium-ion battery anodes, University of Ferrara (2014-2015).

[83] M. Secchi et al., Applied Surface Science 356 (2015) 422 .

[84] A. Andreoli, Porous germanium films as anode materials for lithium ion batteries, University of Ferrara (2015-2016).

[85] E. Garralaga Rojas, Mesoporous Germanium Layer Formation by Electrochemical Etching, PhD Thesis (2010).

[86] S.S. Zhang, Journal of Power Sources 162 (2006) 1379 , Special issue including selected papers from the International Power Sources Symposium 2005 together with regular papers.

[87] D. Lide, Handbook of Chemistry and Physics, 84th Edition (CRC Press, 2003).

[88] http://kbdelta.com/pdf/316-316l-data-sheet.pdf.

[89] J.S. Becker, Chapter 13 - inorganic mass spectrometry of radionuclides, Handbook of Radioactivity Analysis (Third Edition), edited by M.F. L'Annunziata, pp. 833 – 870, Academic Press, Amsterdam, , third edition ed., 2012.

[90] https://www.cameca.com/products/sims/technique.

[91] R.W. Welker, Chapter 1 - basics and sampling of particles for size analysis and identification, Developments in Surface Contamination and Cleaning, edited by R. Kohli and K. Mittal, pp. 1 – 80, William Andrew Publishing, Oxford, 2012.

[92] M. Secchi et al., 2015 IEEE 15th International Conference on Nanotechnology (IEEE-NANO), pp. 522–525, 2015.

[93] J.B. Clegg, Surface and Interface Analysis 17 221, https://onlinelibrary.wiley.com/doi/pdf/10.1002/sia.740170411.